

# JGR Solid Earth

## RESEARCH ARTICLE

10.1029/2022JB024957

### Key Points:

- We construct a new full-waveform tomographic model of the broad Asian region for 30–120 s period via adjoint and spectral-element methods
- The resolution analysis shows reasonably good resolution in the frequency band of interest and limited trade-offs between model parameters
- Our model shed new light on the subsurface behavior of cold subducting slabs & hot mantle flows and their relation to the overriding plates

### Supporting Information:

Supporting Information may be found in the online version of this article.

### Correspondence to:

J. Ma,  
[jma@geophysik.uni-muenchen.de](mailto:jma@geophysik.uni-muenchen.de)







### Citation:

Ma, J., Bunge, H.-P., Thrastarson, S., Fichtner, A., van Herwaarden, D.-P., Tian, Y., et al. (2022). Seismic full-waveform inversion of the crust-mantle structure beneath China and adjacent regions. *Journal of Geophysical Research: Solid Earth*, 127, e2022JB024957. <https://doi.org/10.1029/2022JB024957>

Received 10 JUN 2022  
Accepted 9 SEP 2022

© 2022. The Authors.  
This is an open access article under the terms of the [Creative Commons Attribution License](https://creativecommons.org/licenses/by/4.0/), which permits use, distribution and reproduction in any medium, provided the original work is properly cited.

## Seismic Full-Waveform Inversion of the Crust-Mantle Structure Beneath China and Adjacent Regions

Jincheng Ma<sup>1</sup> , Hans-Peter Bunge<sup>1</sup> , Solvi Thrastarson<sup>2</sup> , Andreas Fichtner<sup>2</sup> , Dirk-Philip van Herwaarden<sup>2</sup>, You Tian<sup>3</sup>, Sung-Joon Chang<sup>4</sup> , and Tingting Liu<sup>5</sup> 

<sup>1</sup>Department of Earth and Environmental Sciences, Ludwig-Maximilians-Universität München, Munich, Germany,

<sup>2</sup>Department of Earth Sciences, ETH Zürich, Zurich, Switzerland, <sup>3</sup>College of Geoexploration Science and Technology, Jilin University, Changchun, China, <sup>4</sup>Department of Geophysics, Kangwon National University, Chuncheon, South Korea,

<sup>5</sup>Geophysical Institute, Karlsruhe Institute of Technology (KIT), Karlsruhe, Germany

**Abstract** We present the first-generation full-waveform tomographic model (*SinoScope 1.0*) for the crust-mantle structure beneath China and adjacent regions. The three-component seismograms from 410 earthquakes recorded at 2,427 stations are employed in iterative gradient-based inversions for three successively broadened period bands of 70–120 s, 50–120 s, and 30–120 s. Synthetic seismograms were computed using GPU-accelerated spectral-element simulations of seismic wave propagation in 3-D anelastic models, and Fréchet derivatives were calculated based on an adjoint-state method facilitated by a checkpointing algorithm. The inversion involved 352 iterations, which required 18,600 wavefield simulations. *SinoScope 1.0* is described in terms of isotropic P-wave ( $V_p$ ), horizontally and vertically polarized S-wave velocities ( $V_{SH}$  and  $V_{SV}$ ), and mass density ( $\rho$ ), which are independently constrained with the same data set coupled with a stochastic L-BFGS quasi-Newton optimization scheme. It systematically reduced differences between observed and synthetic full-length seismograms. We performed a detailed resolution analysis by repairing input random parametric perturbations, indicating that resolution lengths can approach the half propagated wavelength within the well-covered areas. *SinoScope 1.0* reveals strong lateral heterogeneities in the lithosphere, and features correlate well with geological observations, such as sedimentary basins, Holocene volcanoes, Tibetan Plateau, Philippine Sea Plate, and various tectonic units. The asthenosphere lies below the lithosphere beneath East and Southeast Asia, bounded by subduction trenches and cratonic blocks. Furthermore, we observe an enhanced image of well-known slabs along strongly curved subduction zones, which do not exist in the initial model.

**Plain Language Summary** Subduction (a geological process where the oceanic lithosphere descends into the Earth's mantle at convergent boundaries) has been the dominant plate-tectonic process in the broad Asian region since the Mesozoic (252–66 million years ago). The nature of cold subducting slabs and hot mantle flows can record and affect the tectonic evolution of the overriding lithospheric plates. In this study, we conduct the full waveform inversion on a large data set to image the crust-mantle structure of this region. The computationally demanding simulations were performed on two of the world's fastest supercomputing facilities. Our new model delivers seismic illumination of the region at unprecedented resolution and exhibits sharper and more detailed shear wave velocity structure in the lithosphere with greatly improved correlations with surface tectonic units compared to previous tomographic models. The narrow low-velocity layer (generally referred to as asthenosphere) below the lithosphere is present beneath East and Southeast Asia, bounded by subduction trenches and cratonic blocks. The continuous and intense subduction processes are responsible for high-velocity anomalous bodies in the mantle and the formation of the asthenosphere mentioned above.

## 1. Introduction

The late Mesozoic and Cenozoic plate tectonic evolution of the broad Asian region is associated with the north-westward subductions of the Pacific and Philippine Sea plates in the east and the collision and convergence of the Indo-Australian Plate with the Eurasian Plate along the Tethys tectonic belt in the southwest (e.g., Jolivet et al., 2018; Ma et al., 2020; Yin, 2010). The western Pacific Plate began to intersect the East Asian continental margin between 55 and 50 Ma, marked by the demise of the Izanagi Plate. It then started to subduct beneath the Okhotsk and Eurasian plates at a rate of ~8–9 cm/yr along the Kuril and Japan trenches in the north and to descend beneath the Philippine Sea Plate at ~6 cm/yr along the Izu-Bonin-Mariana Trench in the south (Figure 1; e.g., Bird, 2003; DeMets et al., 1994; Hayes et al., 2018). At ca. 20 Ma, it has been suggested that the

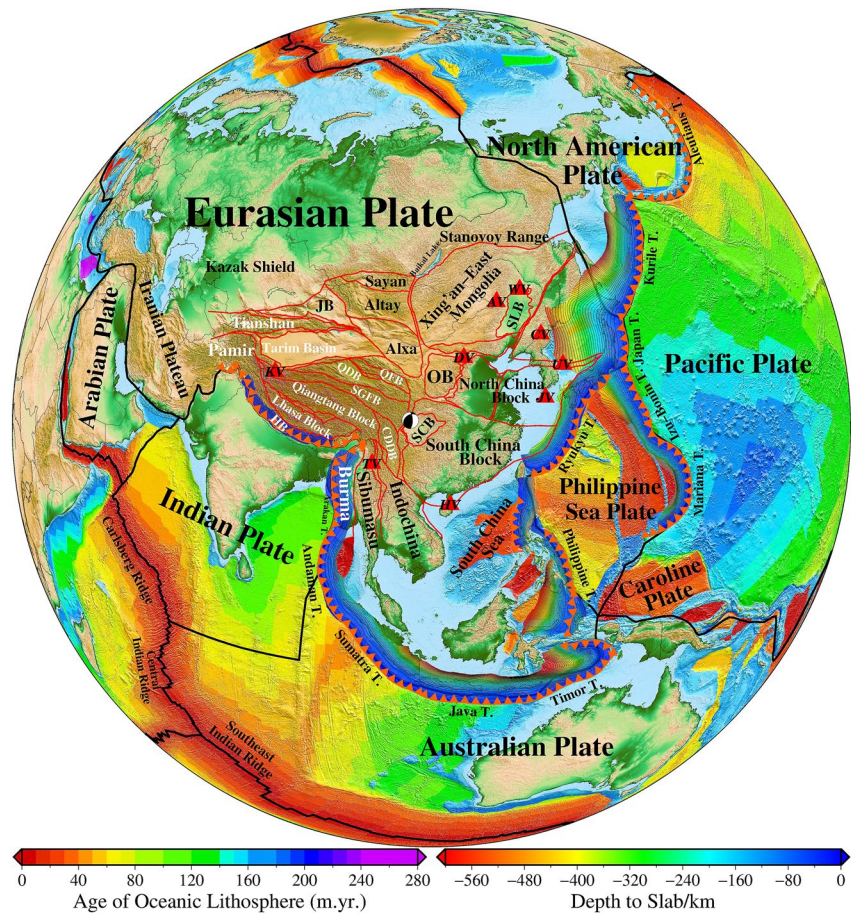


**Figure 1.** Map showing the surface topography and major tectonic features of the broad Asian region. The age-area distribution of the oceanic lithosphere (Seton et al., 2020) is shown in different colors; its scale is shown at the lower left corner below the map. The red triangles mark the active intraplate volcanoes. The red sawtooth lines show the subduction trenches where the oceanic plates are subducting into the mantle. The dark bold lines delineate the major plate boundaries (Bird, 2003), and the red lines define main tectonic units, basins, and large fault zones. The color contour lines show depths to the upper boundaries of the subducting slabs with an interval of  $\sim 20$  km (Hayes et al., 2018), whose scale is shown at the lower right corner below the map. The beach ball denotes the Great Wenchuan earthquake (Mw 7.9, 12 May 2008), which occurred along the Longmenshan Fault, a thrust structure along the border of the Tibetan Plateau and Sichuan Basin. Abbreviations are as follows: AV, Arxan Volcano; CDDB, Chuan-Dian Diamond Block; CV, Changbai Volcano; DV, Datong Volcano; HB, Himalaya Block; HV, Hainan Volcano; JB, Junggar Basin; JV, Jeju Volcano; KV, Kunlun Volcano; OB, Ordos Basin; QDB, Qaidam Basin; QFB, Qilian Fold Belt; SCB, Sichuan Basin; SGFB, Songpan Ganzi Fold Belt; SLB, Songliao Basin; TV, Tengchong Volcano; UV, Ulleung Volcano; WV, Wudalianchi Volcano.

northwestern margin of the Philippine Sea Plate could have collided with the continental margin of the Eurasian Plate along the Nankai Trough and the Ryukyu Trench (e.g., Wu et al., 2016), where it is descending beneath the Eurasian Plate at  $\sim 3\text{--}5$  cm/yr. In the Early Miocene ( $\sim 23$  Ma), an Australian continental promontory began to collide with the Southeast Asian margin of the Eurasian Plate in eastern Indonesia (e.g., Hall, 2011), and now the Australian Plate continues to subduct northwards beneath the Indonesian arcs at  $\sim 5.6$  cm/yr along the Sumatra and Java trenches. The Indian Plate is currently subducting northeastwards beneath Southeast Tibet and the Indochina Block at  $\sim 3.7$  cm/yr, resulting in the shortening and rising of the Tibetan Plateau as well as large-scale continental deformation in the lithosphere extending from the Himalayan orogen to the Baikal rift zone in central Asia (e.g., Tapponnier et al., 1982; Yin, 2010).

Mainland China, as the tectonic transitional zone between the Gondwana and the Laurasia continents, is characterized by the complicated tectonic collage of three major Precambrian blocks (North China Craton, South China Block, and Tarim Block) and ancient continental fragments, separated and sutured by surrounding Phanerozoic orogenic/fold belts (e.g., Zheng et al., 2013). Mainland China also contains a few small cratons and terranes

with diverse origins and complex histories of amalgamation, of which the Ordos and Sichuan blocks, composed of the two rigid continental cores in the East Asia convergent tectonic system, are tectonically relatively stable compared with the adjacent areas. They have suffered less deformation in the long geological history, and may have played an essential role in the formation and tectonic evolution of mainland China. As a result of the unique tectonic setting where the Paleo-Asian, Tethyan, and Paleo-Pacific/Pacific oceanic domains meet in a triangular framework, China is also an active seismic and intraplate volcanic region with significant neo-tectonic activities. According to the USGS Earthquake Catalog (<https://earthquake.usgs.gov>, last accessed June 2022), more than 2,000 earthquakes with a magnitude greater than 5.0 have occurred in mainland China, Japan Islands, and surrounding regions during the last 20 years, for example, the Great 2008 Wenchuan earthquake (Mw 7.9) and the Great 2011 Tohoku-oki earthquake (Mw 9.0). A few active intraplate volcanoes with eruptions during the Holocene exist in mainland China, such as the Arxan, Wudalianchi, and Changbai volcanoes in Northeast China, the Hainan volcano in South China, Tengchong volcano in Southwest China, and the Kunlun volcanic group in northwestern Tibet (Figure 1). The South China Sea, as one of the back-arc basins in the circum-Pacific tectonic domain, is a non-volcanic passive margin basin. Its unique tectonic setting has challenged ideas on the conventional intraplate continental rifting pattern (e.g., Zhang et al., 2020).

Over the past two decades the three-dimensional (3-D) crust and mantle structure beneath the broad Asian region has attracted much attention in seismic studies due to its complicated and unique geological setting involving active lithospheric deformation, intracontinental rifting, intraplate seismotectonics, volcanism and magmatism, continent-continent collision, oceanic plate deep subduction, and mantle dynamics. Following the pioneering works of Aki and Lee (1976), Aki et al. (1977), and Dziewonski et al. (1977), seismic tomography has made substantial progress with the growth of seismic data quality and quantity, and developments in both numerical mathematics and theoretical seismology. Seismic imaging has been the most effective method to detect the 3-D structure of the crust and mantle across a range of scales and enhanced our knowledge of physics, chemistry, and geodynamic processes of the Earth's interior. Many tomographic models, based on various categories of data (e.g., body-wave arrival times, surface-wave dispersion, shear, and surface waveform), have been constructed for East and Southeast Asia (e.g., Chen et al., 2015; Han et al., 2021; Huang & Zhao, 2006; Lebedev & Nolet, 2003; Li & van der Hilst, 2010; Ma et al., 2019; Shen et al., 2016; Tao et al., 2018; Zheng et al., 2008). This has greatly improved our understanding of the plate tectonic and mantle dynamic settings of this region, and its large-scale mantle structure is now well agreed upon. Because of the limitations in the methodology, seismic observation data, and computer powers then available, however, the fine-scale 3-D structure of the crust and mantle beneath China and adjacent regions has not been well established. Although the regional tomographic models can achieve a relatively higher spatial resolution, most are just limited to the shallow upper mantle. Moreover, the models for the same region are usually not consistent due to the differences in the initial reference model, observation data set, and the seismic imaging technique adopted. To address these shortcomings and problems, we collected a large number of waveform data sets across the broad Asian region to construct a reference seismic model. It should be a crucial step in enhancing our understanding of the subsurface behavior of cold subducting slabs and hot mantle flows and their dynamic relation to the tectonic evolution of the overriding plates as mentioned above.

With recent advances in numerical methods and high-performance computing (e.g., Afanasiev et al., 2019; Gokhberg & Fichtner, 2016; Komatitsch & Tromp, 2002a; 2002b), it has become computationally feasible to improve images of the Earth's interior using numerical forward and adjoint simulations of seismic wave propagation through 3-D heterogeneous Earth models in iterative inversions, ranging from regional and continental (e.g., Chen et al., 2015; Fichtner et al., 2009; Krischer et al., 2018; Tape et al., 2009; Zhu et al., 2012) to global scale (e.g., Bozdağ et al., 2016; French & Romanowicz, 2014; Lei et al., 2020; Lekić & Romanowicz, 2011). Synthetic seismograms calculated by finite-element or finite-difference methods contain the full seismic wavefield information, including all body and surface wave phases as well as scattered waves generated by lateral variations of the model physical properties. Therefore, the amount of exploitable information used in full-waveform inversion (FWI) is significantly larger, which provides new opportunities for improving images of the Earth's interior. However, relying on accurate numerical wavefield simulations, FWI is not applied as widely as other traditional techniques, such as ray-based travel-time tomography (e.g., Grand et al., 1997; Li et al., 2008; Ma et al., 2019; Zhao, 2004; Zhao et al., 1992) and finite-frequency tomography (e.g., Dahlen et al., 2000; Hosseini et al., 2020; Hung et al., 2000; Montelli et al., 2004). This primarily stems from the substantial computational requirements since FWI via the adjoint-state method requires two numerical simulations of the wave equation for each source at each iteration to obtain the gradient of the misfit with respect to the model parameters. Additionally,



the computational cost of the simulation scales with frequency to the power of four in a 3-D medium (e.g., Thrastarson et al., 2020; Virieux & Operto, 2009). The Fresnel zone of the higher-frequency wave is narrower because of divergence decreasing with increasing frequency, and as a consequence, more events are required to construct a more accurate gradient in order to constrain the physical properties of the Earth model sufficiently. To this end the dynamic mini-batch optimization, conceptually related to the stochastic gradient descent method, is an effective strategy that can drastically reduce the computational burden of real-data FWI applications (e.g., Boehm et al., 2018; Matharu & Sacchi, 2019; van Herwaarden et al., 2020; van Leeuwen & Herrmann, 2013).

The dense deployment of temporary and permanent broadband seismic stations in mainland China and adjacent regions (e.g., ChinArray project, China Digital Seismic Network, Korea National Seismograph Network, F-net Broadband Seismograph Network) in the past two decades provides notable advantages to construct a new tomographic model of the crust-mantle structure beneath the broad Asian region, using FWI of three-component (vertical, radial, and transverse) recordings. Moreover, in agreement with the collaborative and evolutionary framework for the construction of a multi-scale seismic model (Fichtner et al., 2018), the final result of this work will flow back into the Collaborative Seismic Earth Model (CSEM), which can further serve as a foundation for future generations of 3-D reference Earth models. Such models would be crucial to accurately locate earthquakes, invert earthquake sources, assess seismic hazards in earthquake-prone regions, assist accurate earthquake early-warning, and detect and locate nuclear explosions. They would also be important to refine plate tectonic studies in the coming years (Wu et al., 2016).

## 2. Seismic Data

From the Global Centroid Moment Tensor (GCMT) solution database (Ekström et al., 2012), we selected  $\sim 2,500$  earthquakes within the moment-magnitude range  $5.0 \leq M_w \leq 6.9$  in the domain of interest. The lower bound of the magnitude range is chosen to provide a high signal-to-noise ratio in useable recordings. The upper bound is empirically chosen to neglect finite-source effects in seismogram modeling. All events occurred between January 2009 and October 2018. Moreover, they were chosen to evenly distribute in seismogenic zones associated with active subductions, Mid-ocean ridges, and tectonic deformation and faulting (Figures 1 and 2).

We obtained three-component seismograms from nearly all available permanent broadband seismic networks in mainland China (CEArray, <https://www.seisdmc.ac.cn/>; Zheng et al., 2010), South Korea (KNSN, <http://www.kma.go.kr/>), Japan (F-net, <http://www.fnet.bosai.go.jp/>), and other regional and global temporary broadband seismic networks, made available by the Incorporated Research Institutions for Seismology Data Management Center (IRIS DMC, <http://ds.iris.edu/ds/nodes/dmc/>). To enable better performance and fast parallel processing on high-performance clusters, the Adaptable Seismic Data Format (ASDF; Krischer et al., 2016) serves as a data container in this study. It combines all seismic traces, the event information file (in QuakeML format), and the station information file (in StationXML format) for an event into a single file using the HDF5 format. The adjoint method is maximally efficient for cases with a sizable seismogram-to-event ratio. Also the computational cost for forward and adjoint simulations does not depend upon the number of receivers. Hence we preferentially choose events with the maximum number of high-quality seismic recordings in similar locations. To optimize the seismic wavefield azimuthal coverage, we employ earthquakes located in all azimuths with respect to CEArray stations, which are the key component of our data set. With a total of 2,427 available seismic stations and 410 seismic sources, our final data set contains more than 0.5 million three-component seismograms, resulting in tremendous amounts of high-quality recordings from  $\geq 1,300$  unique stations per event. The distribution of events, seismometers, and the surface-projected ray coverage are illustrated in Figure 3. Although the sensitivity of the measurements in FWI is not restricted to the ray paths, the data coverage determines the first-order features of a tomographic result, making a surface ray density plot a useful proxy to judge the potential resolution of the final model. It shows, for instance, that mainland China, the India-Eurasia collision zone, the Philippine Sea Plate, as well as the western Pacific and the Indonesia subduction zones are well covered in our region of interest.

## 3. Forward and Inverse Modeling

We perform seismic waveform modeling and inversion mainly based on the methodology established in Fichtner (2011), Kennett and Fichtner (2020), and similar works (e.g., Colli et al., 2013), which is depicted schematically in the workflow shown in Figure 4. We introduce some technical details of the initial model, seismic waveform modeling, optimization, and workflow management in the following sections.



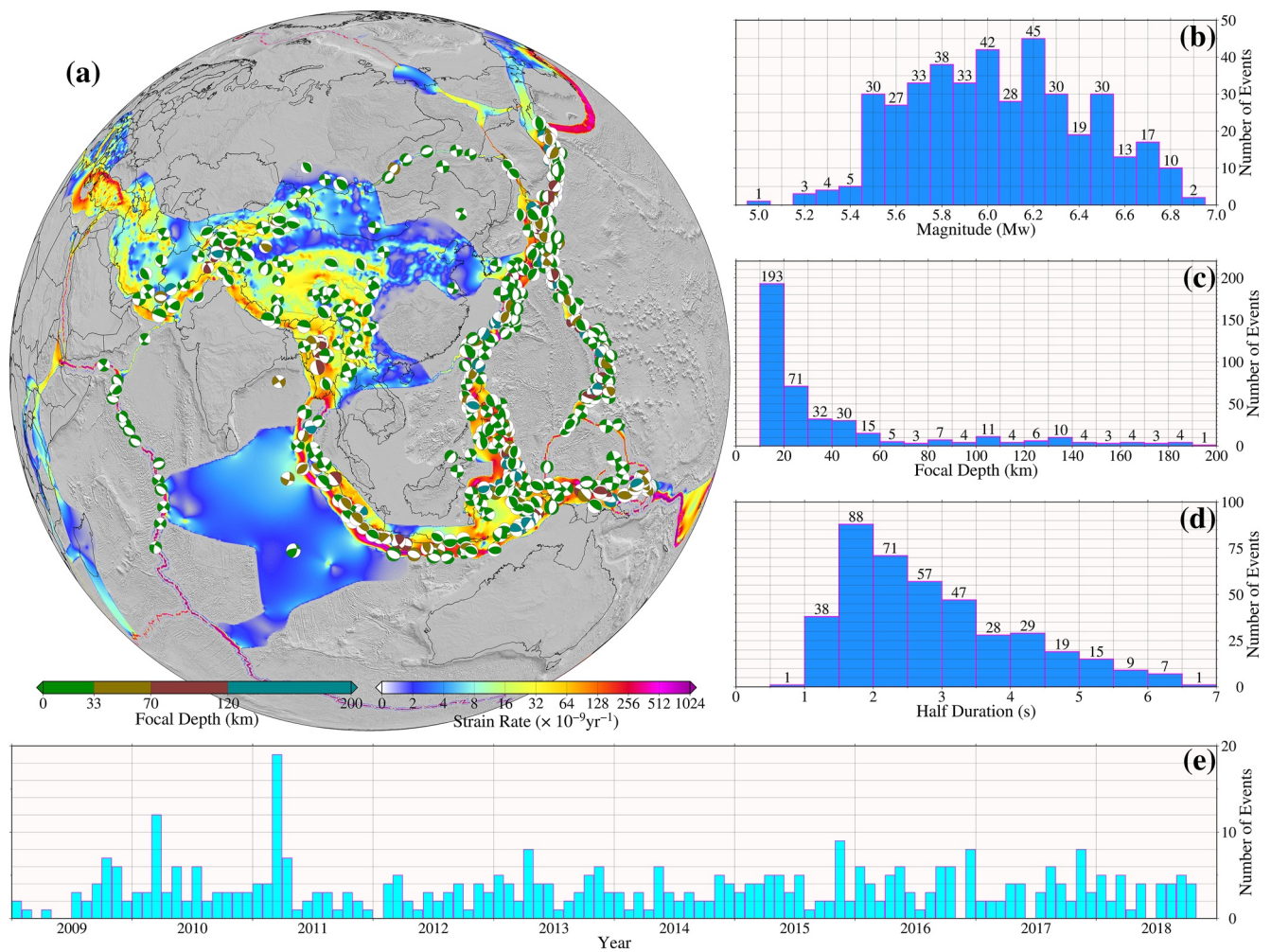


**Figure 2.** 410 earthquakes used for the full-waveform inversion in this study. (a) Distribution of 410 earthquakes. The colors of moment tensor beach balls denote the focal depths, whose scale is shown at the lower left corner below the map. The strain rates are inverted from GPS measurements (Kreemer et al., 2014). The color scale is not linear and saturated at high values, whose scale is shown at the lower right corner below the map. (b–e) Histograms of earthquake moment magnitudes, focal depths, half durations, and origin times.

### 3.1. Starting Model and Numerical Waveform Modeling

It is well known that FWI is a large nonlinear minimization problem that can only be solved efficiently with iterative gradient-based minimization schemes, during which each iteration involves a minor update constructed through linear operations on the residuals. An accurate starting model can help avoid convergence toward a local minimum or saddle points, increase the length and number of measurement windows at the beginning stage of the inversion, and accelerate the convergence of the iterative inversion toward the global minimum. Therefore, we implement a 3-D initial model that contains the long-wavelength features of the crust and mantle beneath the broad Asian region, extracted from the CSEM (Afanasiev et al., 2016; Fichtner et al., 2018). The background model of the CSEM was constructed from the 3-D long-wavelength S-velocity model S20RTS (Ritsema et al., 1999), with P-velocity variations derived from a depth-dependent P-to-S scaling relation (Ritsema & van Heijst, 2002). The initial crustal model was derived from the model of Meier et al. (2007a, 2007b), which includes estimations of both S-wave velocity and crustal thickness. The initial model additionally contains contributions from previous FWI models of Japan (at periods down to  $T = 20$  s; Simuté et al., 2016) and Australia (at periods down to  $T = 30$  s; Fichtner et al., 2010). The model for wave propagation simulations is parameterized in horizontally and vertically propagating/polarized P and S velocities ( $V_{PH}$ ,  $V_{PV}$ ,  $V_{SH}$ ,  $V_{SV}$ ), mass density ( $\rho$ ), shear attenuation ( $Q_{\mu}$ ), and the dimensionless parameter ( $\eta$ ), which is used to control the dependence of P and S velocities on the incidence angle (Dziewonski & Anderson, 1981).

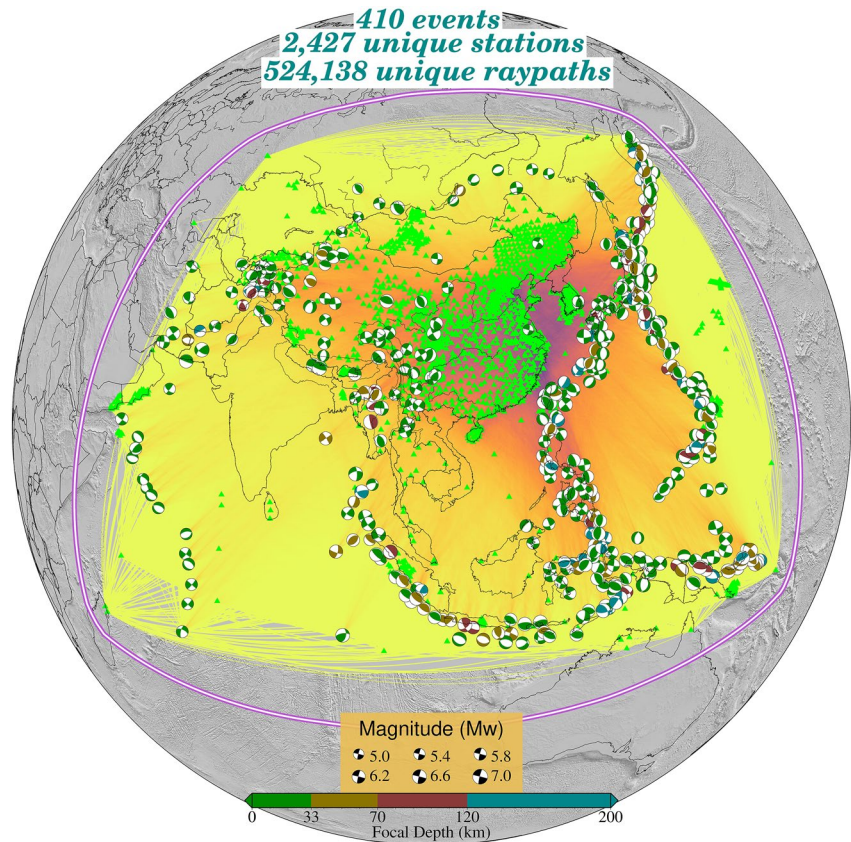


**Figure 3.** Surface-projected ray density map of the events and stations used in this study, ranging from dark red (best data coverage) to light yellow (least data coverage). Earthquake locations and mechanisms are indicated by moment tensor beach balls and stations by green triangles. In total, 410 earthquakes were recorded at 2,427 unique stations, and the complete data set has 524,138 unique source-receiver pairs. The outer boundary marks the start of the absorbing boundary region. The great circle paths of all traces used in this study are located within the outer boundary, which can mitigate the influence of the absorbing boundary on the inversion.

FWI is an efficient method to extract information from complete seismic waveforms and recover the “best fit” model by iteratively minimizing the cumulative misfit between observed and synthetic seismograms from forward modelings. It guarantees that the observed waveform misfits are generated by the undiscovered Earth structure and not by approximation errors, and further avoids approximation artifacts from the forward modeling. In this study, accurate numerical solutions of the visco-elastic wave equation in a radially anisotropic Earth media are computed with the spectral-element seismic wave propagation solver Salvus (Afanasiev et al., 2019) accelerated by Graphics Processing Units. Salvus is a suite of highly parallelized software performing full-waveform modeling and inversion across all scales. Due to the non-uniform geometry of seismic networks and uneven distribution of seismic sources, an adaptive mesh is adopted for seismic wave propagation simulations to reduce the computational burden (Figure 3).

### 3.2. Misfit Function and Optimization Scheme

Seismic tomography allows us to infer Earth's internal structure from the misfit measurements between observed and synthetic data. The choice of a suitable misfit function that quantifies the differences between synthetic and observed waveforms and extracts the maximum amount of meaningful information from each seismogram plays an important role in the outcome of an inversion. The dependence of seismic amplitude characteristic attributes on variations in the medium properties is usually highly nonlinear. The absolute amplitudes are strongly influenced by local anomalies near the receiver, and important information about the deep Earth can be masked by shallow structures such as sedimentary basins (Fichtner et al., 2010). In contrast, phase differences are quasi-linearly related to 3-D Earth structural variations and so are well suited for an iterative gradient-based misfit minimization

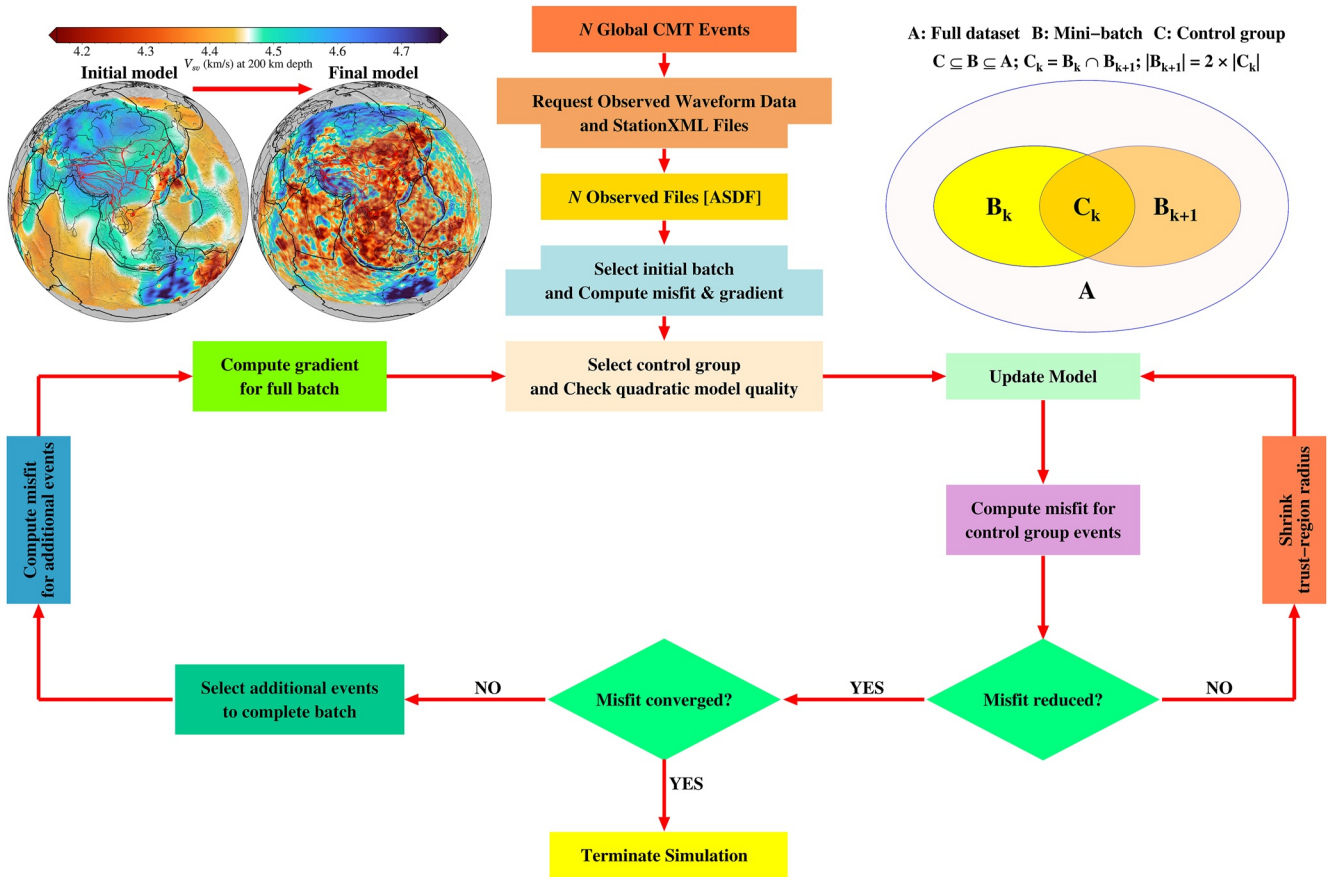


**Figure 4.** Schematic representation for the stochastic-gradient mini-batch full-waveform inversion. Mini-batch  $B_k$  for the iteration  $k$  is a subset of the complete data set  $A$ , and the mini-batch for the next iteration  $k + 1$ ,  $B_{k+1}$ , consists of the control group  $C_k$ , a subset of  $B_k$  as well as other events, which are quasi-randomly chosen from the complete data set  $A$ . It starts with the preparation of observed waveform data, as discussed in Section 2, and assembles the complete data set in the initialization stage. We select the first mini-batch using Mitchell's best candidate algorithm, calculate the synthetic seismograms, misfits, and gradients with a suitable initial model, and update the model. At the next iteration, we select the control group events from the previous mini-batch and recalculate misfits of the control group events with the updated model. If misfits are reduced at this stage, new events from the complete data set are selected to complete the next mini-batch, for which misfits and gradients are then again calculated with the updated model. This procedure is iterated until a satisfactory fit is achieved.

scheme. Here we work with the phase misfit measure in the time-frequency domain (e.g., Fichtner et al., 2008; Kristeková et al., 2006; Kristeková et al., 2009). The phase misfits do not require the identification and isolation of individual seismic phases, and are naturally applicable to any kind of seismic wave, regardless of its composition of seismic phases. The total phase misfit  $\chi_p^2$  is defined by an integral over all phase differences in the time-frequency domain as

$$\chi_p^2 = \int_t \int_\omega W^2(t, \omega) [\Theta_{syn}(t, \omega) - \Theta_{obs}(t, \omega)]^2 dt d\omega, \quad (1)$$

$$W = \frac{\log(1 + |\tilde{u}_{obs}|)}{\max(\log(1 + |\tilde{u}_{obs}|))},$$

where  $W$  is the weighting function,  $\tilde{u}$  is the time-frequency representation of seismic signal  $u$  as calculated via the Gabor transform, and  $\Theta_{syn}$  and  $\Theta_{obs}$  are the phase of the synthetic and the observed seismogram traces. For a derivation of this misfit functional and corresponding adjoint source, see Fichtner et al. (2009) and Fichtner (2011).

To reduce the effect of clustering on the sensitivity of Fréchet kernels across the domain of interest due to the uneven distribution of seismic stations, we employ the geographical weighting strategy, which empirically leads to faster convergence of nonlinear inversions. To this end, the final misfits for a given receiver location  $x_r$  are multiplied by the factor



$$W_r = \left( \sum_{i=1, i \neq r}^n \frac{1}{|x_i - x_r|} \right)^{-1}. \quad (2)$$

We select measurement time windows in a semi-automatic fashion utilizing a sliding window cross-correlation, where initial windows are preselected based on the noise level and the overall similarity between observed and synthetic waveforms. This yields time-dependent cross-correlation coefficients and time shifts, which are further combined with specific criteria to determine the final time windows (e.g., Krischer et al., 2015; Maggi et al., 2009; Thrastarson, van Herwaarden, Krischer, & Fichtner, 2021). Subsequently, the selected time windows are manually checked and adjusted to avoid cycle skipping, especially for the high-frequency signals used in the final inversion stage. As the iterations progress, the number of selected time windows for each event and the number of traces with windows increase almost exponentially from the long to the short period bands.

Our gradient-based optimization scheme iteratively improves the model to reduce the waveform misfit between iterations. To achieve an optimal global solution and mitigate the risk of convergence toward a local minimum, we divide the whole inversion procedure into three successively broadened period bands of 70–120 s, 50–120 s, and 30–120 s. This implies a multi-scale evolutionary inversion scheme of starting with the long period to determine large-scale structure before marching into the higher-frequency domain to reveal the small-scale structure (e.g., Bunks et al., 1995; Krischer et al., 2018). We calculate sensitivity kernels of the cumulative phase misfit with respect to the model parameters for each individual event through the adjoint method (e.g., Fichtner et al., 2006; Tarantola, 1988; Tromp et al., 2005). To reduce the parameter space, we enforce  $\eta = 1$  and  $V_{PH} = V_{PV}$  and invert only for the isotropic P velocity ( $V_p$ ), the velocity of horizontally polarised S waves ( $V_{SH}$ ), the velocity of vertically polarised S waves ( $V_{SV}$ ), and mass density ( $\rho$ ) simultaneously over the course of the inversion's three stages. The other parameters are kept at the initial values of the starting model throughout the inversion.

In this study, we decided against inverting for the earthquake sources but assume the centroid-moment tensor solutions from the GCMT catalog (Ekström et al., 2012) to be correct for two main reasons: (a) we use rather long-period waves (30–120 s), so our inversion is not affected much by errors in them; (b) our inversion domain is not a global scale, and it means that any inversion for source mechanisms will likely incur a bias from imperfect azimuthal coverage, especially for those events close to the border of the computational domain. The global full-waveform source inversion for the source parameters from the GCMT catalog shows that they generally change by less than 5 km in depth and less in the lateral directions (Bozdağ et al., 2016), which only make tiny contribution to the waveform fit. In order to further mitigate the potential bias from source errors, for each event, it is crucial to remove source and receiver imprints from the raw gradient since they generally show strong localized sensitivity in these areas. In addition, the raw gradient usually contains small-scale oscillations and high-frequency artifacts, and it is essential to prevent these sub-wavelength structures from sneaking into the model by effectively convolving the gradients through the numerical solution of the diffusion equation (e.g., Afanasiev et al., 2019). The smoothed gradient determines the descent direction, which is used to compute a model update through suitable optimization algorithms. The Limited-memory BFGS (L-BFGS) is a quasi-Newton method of optimization, which utilizes curvature information based on approximation of the Hessian (the second derivative of the misfit) and its inverse constructed from the gradients and models of previous iterations (Liu & Nocedal, 1989; Nocedal & Wright, 1999). The L-BFGS combined with the trust-region method (Conn et al., 2000; Nocedal & Wright, 1999) can achieve a good approximation of the local objective function and significantly reduce the cost of an FWI update, which makes it greatly attractive for solving large-scale inverse problems. In this study, we performed all iterations based on the dynamic mini-batch approach coupled with the trust-region L-BFGS optimization technique (van Herwaarden et al., 2020). It is particularly well suited for our domain of interest for the following reasons: (a) the presence of redundancies in the data set because seismic sources tend to reoccur in similar locations, such as subduction zones. This limits the amount of new independent information to the gradient direction. (b) the large amount of continental-scale data set for 410 seismic sources. This poses a significant challenge for the computational requirements faced in real-data FWI applications. Different from conventional FWI or mono-batch FWI, which considers the data set as a whole in each iteration, the dynamic mini-batch FWI quasi-randomly selects a subset of the complete data set with the help of Mitchell's Best-Candidate algorithm (Mitchell, 1991) to approximate the complete gradient. It is specifically tuned to deal with redundancies in seismological data sets, potentially reducing the computational cost significantly (for details, see van Herwaarden et al., 2020, 2021).

### 3.3. Workflow Management

The FWI workflow based on the adjoint method consists of a series of iterations. Each is composed of a significant number of operations (e.g., construct, submit, and monitor forward and adjoint simulations for each seismic source, select measurement windows and calculate misfits between the observed and synthetic data, pre-processing and construction of adjoint sources, pre-processing and smoothing of gradient data, nonlinear optimizations, and model updates). One of the main challenges faced in large-scale FWI applications is to increase the quality and resolution of seismic models with massive data volumes in a reliable and trustworthy manner while keeping the time to solution as short as possible. Workflow management helps to automate the whole workflow by cutting down human interaction as much as possible, especially when performing repetitive tasks. To this end, we employ the FWI workflow manager *Inversionson* to fully automatically perform the above tasks until the convergence criteria of the whole inversion can be properly reached (for details, see Thrastarson, van Herwaarden, & Fichtner, 2021). This workflow engine also automatically detects job failures and facilitates tracking of tasks and automatic job resubmission when necessary.

## 4. Model Assessment

In this section, we analyze the quality of the first generation full-waveform tomographic model *SinoScope 1.0*. First, we present the iterative model evolution through three successively broadened period bands. Then we present examples of the waveform fit for a few events and stations relative to the initial and final models. Finally, we perform a computational expensive resolution test to estimate the resolution for the final model and the trade-offs between model parameters.

### 4.1. Model Evolution

For three successively broadened period bands of 70–120 s, 50–120 s, and 30–120 s in this study, the raw waveform data are corrected for the instrument responses to obtain the ground displacement and be filtered to match the spectral content of the synthetic data using ObsPy (Krischer et al., 2015; Megies et al., 2011) during the respective stages of the inversion. We first invert for the long-wavelength structures from the low-frequency waveforms and progressively toward higher-frequency waveforms for the shorter-wavelength structures, thereby avoiding strong dependence on the initial model and preventing the optimization procedure from getting trapped in local minimum.

The multi-scale FWI scheme coupled with the dynamic mini-batches is a journey of continuously and steadily resolving fine-scale structures of the Earth's interior through forward and adjoint simulations. The drawback of the gradient-based optimization scheme is that it improves the models slowly with slight differences between iterations. Even significant reductions in misfit value may do not cause apparent improvement in the model parameters. For the longest-period stage A (70–120 s) at a substantially low computational cost, we performed 147 iterations, corresponding to 6,264 simulations of the forward plus adjoint on the numerical meshes with 272,471 elements (Figure 5). As the iteration progressed, we gradually increased the minimum control group size to provide a more accurate search direction, reducing the risk of the model's frequent rejection in the optimization. The  $L_2$  difference between the current and initial models increases rapidly as the large-scale structure is well recovered during the first few dozen iterations and has been gradually stagnant in the final iteration stage, where more simulations would not have significantly improved model parameters. For stage B (50–120 s), we performed 168 iterations, corresponding to 4,888 simulations on the numerical meshes with 598,908 elements when the  $L_2$  curve stagnated, and the inversion was forced to be terminated (Figure 5). For the shortest-period stage C (30–120 s), it is necessary to employ smaller elements and a shorter time step to resolve the smaller-scale structures. The computational costs are proportional to the number of elements and time steps. As a consequence, a single simulation of stage C is more than 20 times as expensive as a single one for stage A. We performed 41 iterations, corresponding to 7,448 simulations on the numerical meshes with 2,290,274 elements as the  $L_2$  curve stagnated (Figure 5). Most notably, the trend of the  $L_2$  curve, to a certain extent, broadly fluctuates in the early stage, which is probably because 410 events have not been wholly used to contribute their unique information to the gradient direction, and after that starts to become relatively smooth (Figure 5).

Figure 6 shows the model evolution with horizontal slices of the vertically polarised shear velocity at a depth of 100 km as a function of simulations at three different stages. For each stage of the multi-scale inversion, as

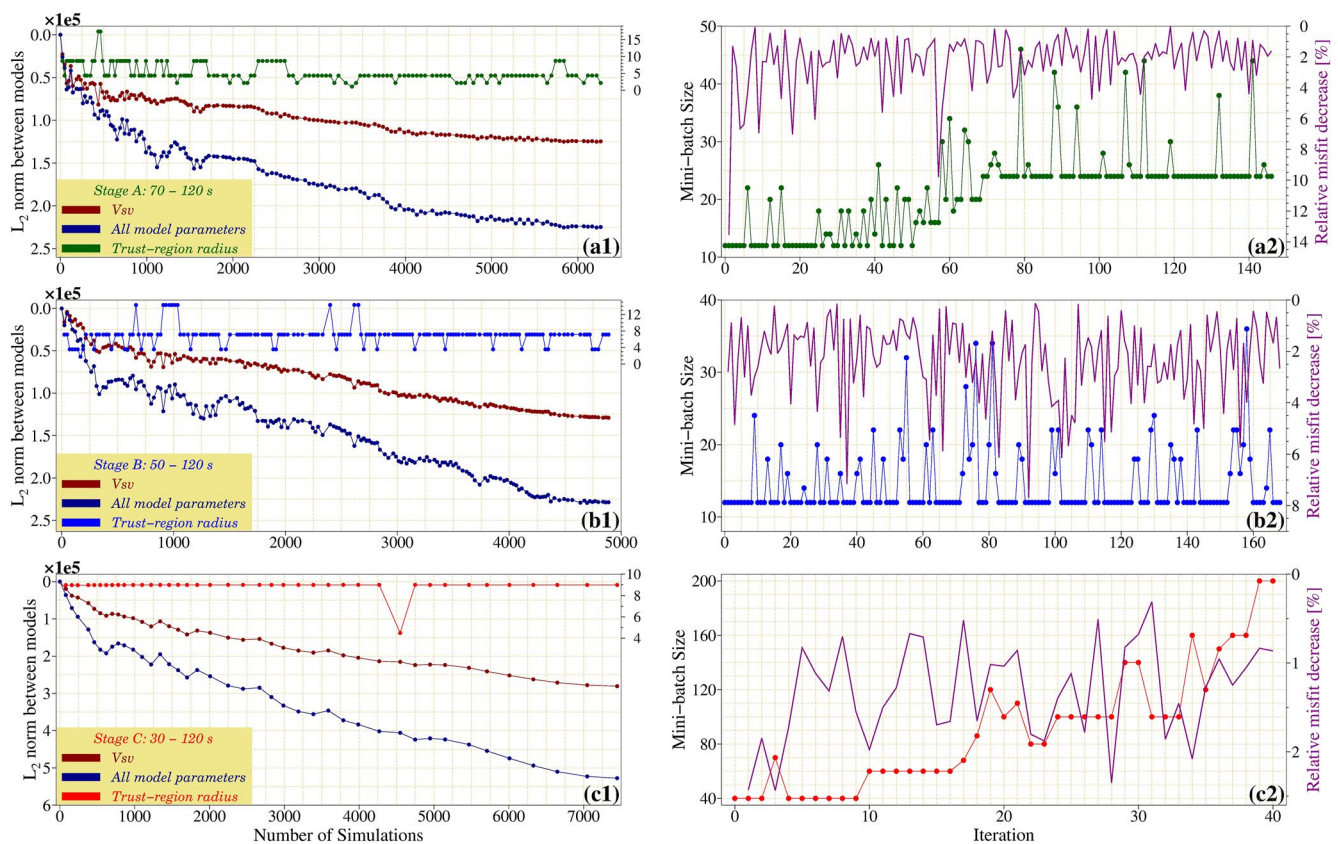


**Figure 5.** (a1–c1) Per-iteration  $L_2$  distance between the initial and later models, and the trust-region radius used in the optimization for the three successively broadened period bands of 70–120 s (green), 50–120 s (blue), and 30–120 s (red). Note the general trend of  $L_2$  distance gradually increasing. (a2–c2) Evolution of the mini-batch sizes and the relative misfit decrease of the control groups over the course of the inversion's three stages. Since the mini-batch size is closely related to the allowable angular difference, it automatically changes during the inversion to contribute more unique gradient information with the lowest possible computational cost. More events are required to approximate the complete gradient at the short period (30–120 s), because the Fresnel zone of the higher-frequency wave is narrower. Note the different axes.

it extends to shorter periods, the later stage keeps adding substantially more details into the model, which is precisely what we expected. FWI naturally inverts body and surface waves, which can combine the advantages of these two data types. The incorporation of surface waves can greatly reduce the vertical smearing effect that is typical for pure body-wave tomography in the upper mantle. Body waves provide additional lateral resolution at greater depths than pure surface-wave tomography can achieve. As illustrated in Figure 7, with the introduction of a large amount of body wave measurements in the inversion at the shorter periods, the deep structure of the model has been dramatically improved compared to the initial model.

#### 4.2. Waveform Fits

In this section, we use waveform comparisons between initial and final models as well as the ability of the final model to explain the test data set to estimate the validity of the final model. Waveform comparisons were performed for selected source-receiver pairs that sample the study area along differently oriented ray paths. Figure 8 shows 12 representative examples of the improved match between observed and synthetic three-component recordings from the test data set used in the inversion for the initial versus the final model. The total time window length of the fitted portions has increased by over an order of magnitude, with more than 70% misfit reduction compared with the original time windows. Also, note that the final model can explain body waves and fundamental- and higher-mode surface waves significantly better than the initial model. For most events, the amplitude fit improves along with the phase, although we did not explicitly invert the amplitude information.

We use a test data set including stations with the epicentral distance range of 50°–70° that were not used in the above inversion, to further assess the quality of the final model and identify if the data has not been overfitting



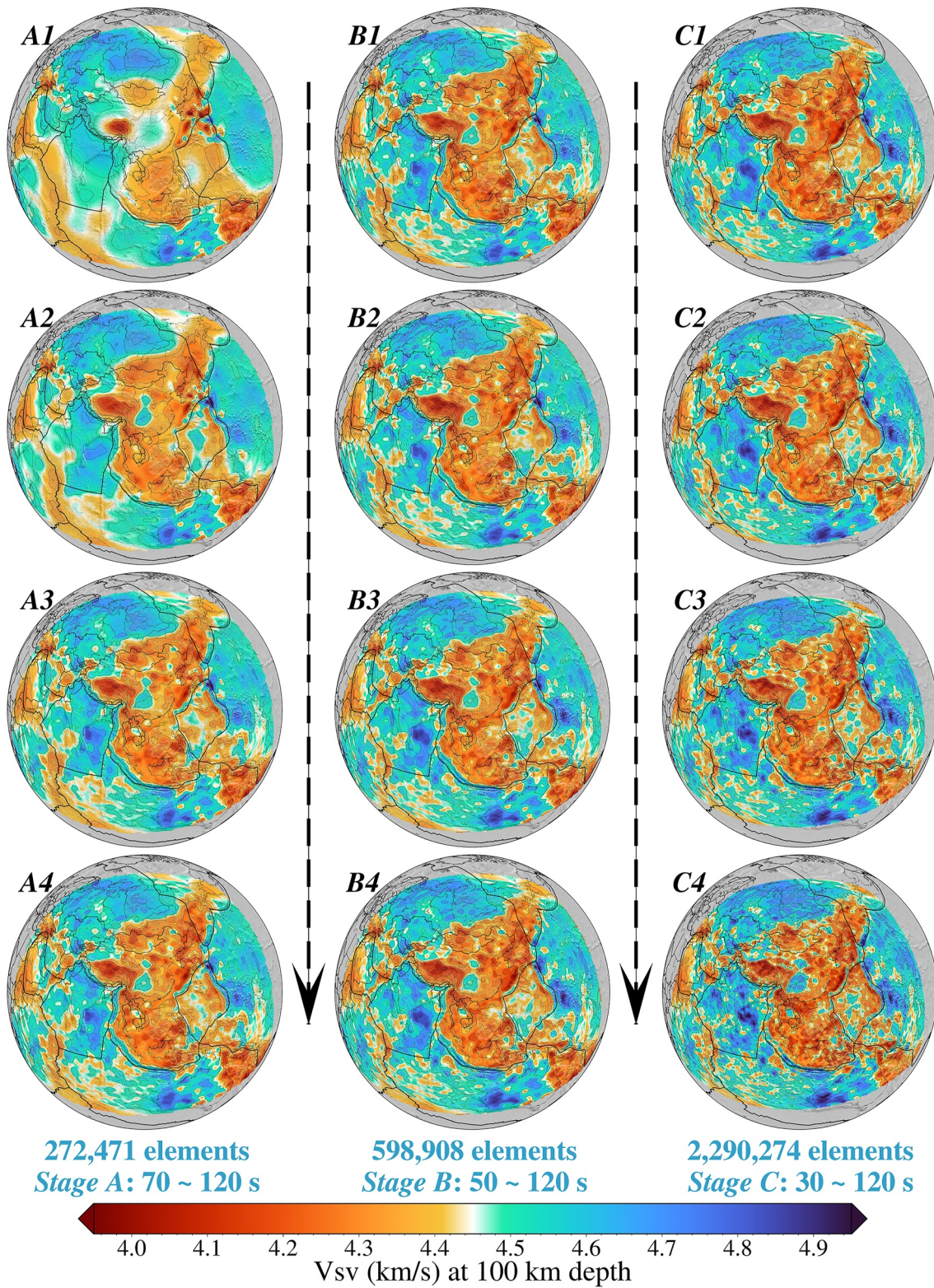
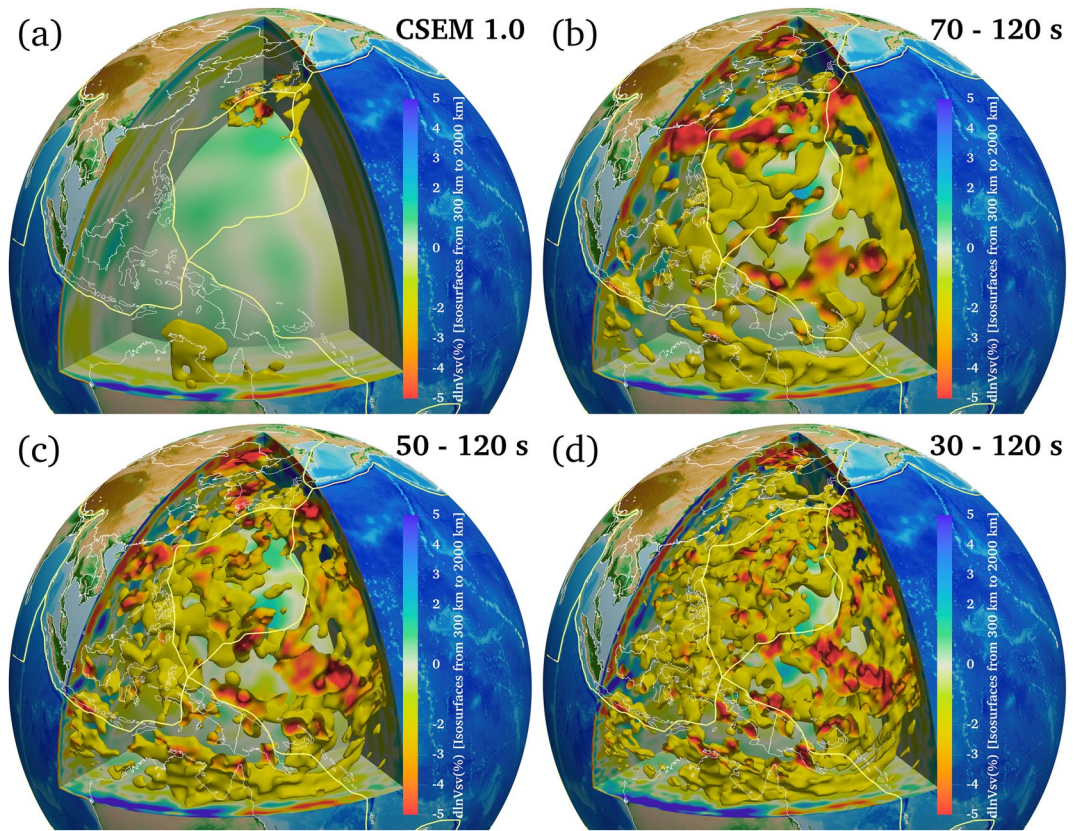


Figure 6.





**Figure 7.** 3-D visualizations of the slow vertically polarized shear wave velocity structure (with  $V_{sv}$  perturbations  $\leq -2\%$ ) beneath the eastern Asian regions in starting model Collaborative Seismic Earth Model (a), stage-A final model (b), stage-B final model (c), and stage-C final model (d) from a depth of 300 km to a maximum depth of 2,000 km. As the frequency increases, more body waves measurements are introduced in the inversion processes, and the seismic velocity structure of the Earth's deep interior is portrayed more and more finely. The color scale is identical for all plots, and each model is plotted relative to the lateral mean of the stage-C final model.

significantly. We first remove the observed data traces with no visible earthquake signal and adopt the normalized waveform difference  $L_2$  misfit instead of the time-frequency phase misfit to measure all parts of observed and synthetic waveforms on all three components only for the fitted portions over all stations (e.g., Krischer et al., 2018; Simutè et al., 2016; Tape et al., 2010).

$$\chi(\mathbf{m}) = \frac{\int_0^T [u_{obs}(t) - u_{syn}(t, \mathbf{m})]^2 dt}{\sqrt{\int_0^T [u_{obs}(t)]^2 dt \int_0^T [u_{syn}(t, \mathbf{m})]^2 dt}} \quad (3)$$

where  $u_{obs}$  and  $u_{syn}$  are observed and synthetic waveform traces,  $T$  is the duration of the time series, and  $\mathbf{m}$  is the model which the synthetic data is calculated with.

Figure 9 provides an exemplary comparison of synthetic three-component recordings with a duration of 3,600 s for the newly added events, calculated through the initial and the final models with the same mesh accuracy as the stage C. Synthetic seismograms improve significantly compared to observed seismograms when going from the initial to the final model. The average per-trace misfit  $\bar{\chi}$  for the test data set calculated with the initial

**Figure 6.** Horizontal slices of the models at different stages of the inversion. Shown are vertically polarized shear wave velocity ( $V_{sv}$ ) distributions of the models at 100 km depth across the model domain. A1: the initial model for stage A (Fichtner et al., 2018); A2, A3, and A4: the dynamic mini-batch full-waveform inversion (FWI) results after 2,068, 4,180, and 6,264 simulations (forward plus adjoint). B1: the initial model for stage B, interpolated from model A4; B2, B3, and B4: the dynamic mini-batch FWI results after 1,640, 3,264, and 4,888 simulations. C1: the initial model for stage C, interpolated from model B4; C2, C3, and C4: the dynamic mini-batch FWI results after 2448, 4,948, and 7,448 simulations. The dynamic mini-batch iterations at the long periods mainly adjust the long-wavelength structure, and more fine-scale details appear during later iterations at short periods.

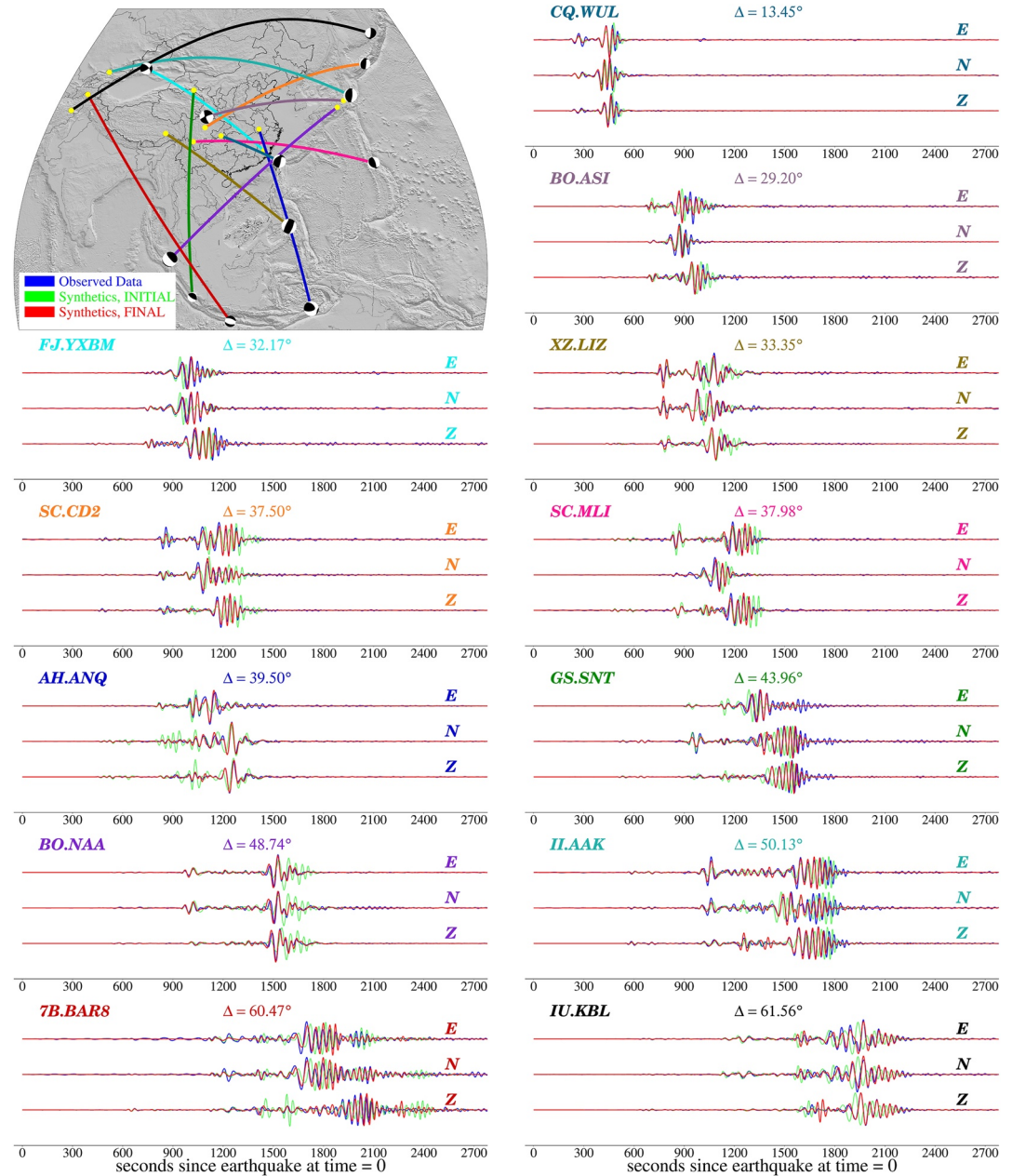


**Figure 8.** Comparisons of the overall waveform fit between synthetics calculated with the initial model Collaborative Seismic Earth Model as thin green lines, synthetics calculated with the stage-C final model as thick red lines, and the observed waveforms as thick blue lines for the event for which raypaths are shown in the topographic map with the same corresponding seismometer colors next to the seismograms. Epicenters are marked by beachballs in the topographic map, while solid yellow dots denote stations.

model is 2.15, which is considerably bigger than a value of 0.72 calculated with the final model. It indicates the model was greatly improved throughout the inversion. Based on the visual and quantitative analyses, we conclude that numerous simulations produced a well-improved model, which may be used to assist accurate earthquake early-warning and invert earthquake sources in the coming future.

### 4.3. Resolution Analysis

It is not possible to calculate the exact spatial resolution in the large-scale nonlinear inversion because there does not exist a simple mathematical operator relating the inversion input and output. In the absence of quantitative



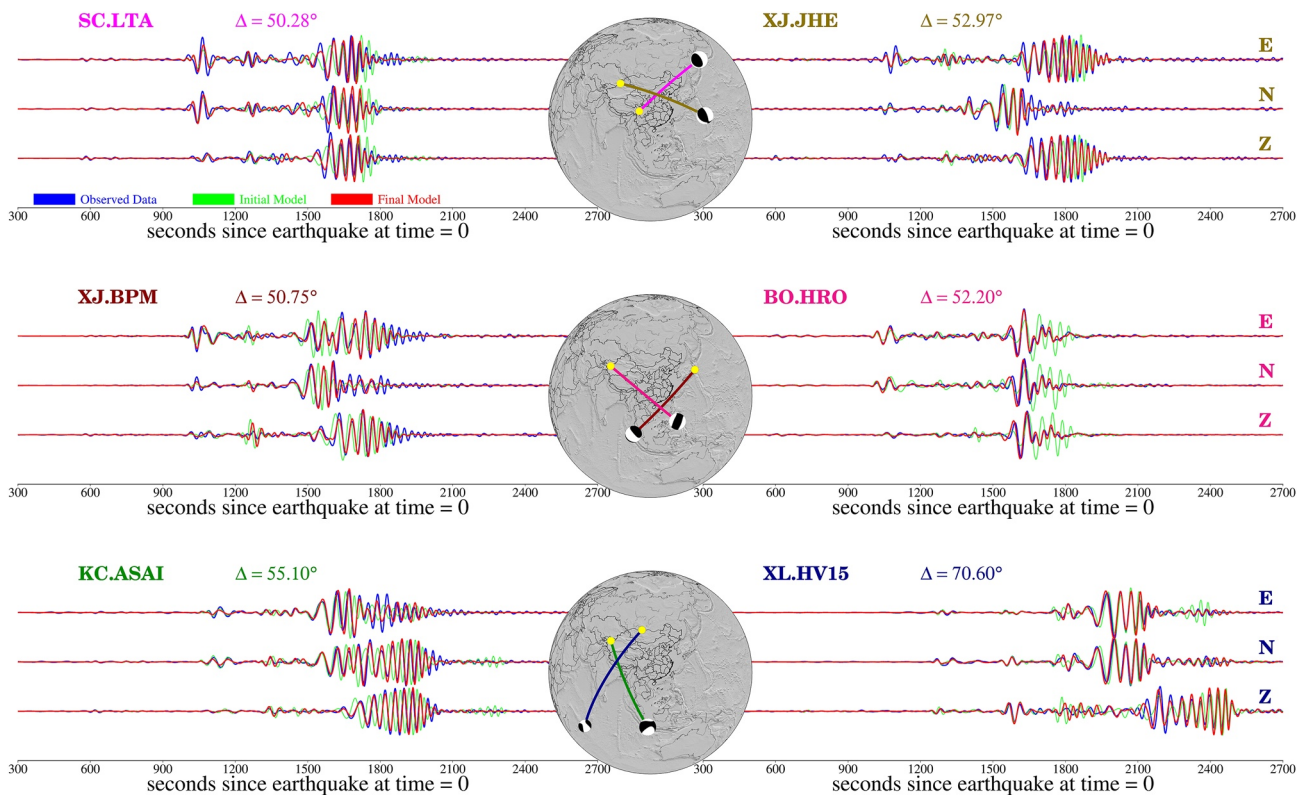


**Figure 9.** Representative waveform comparisons for several events from the test data set to assess the ability of the final model to explain new waveform data not used in the inversion. Waveform amplitudes are not scaled in order to compare the difference of waveform data more objectively. The observed waveforms are plotted as thick blue lines, synthetics calculated with the final model as thick red lines, synthetics calculated with the initial model as thin green lines, both of which are simulated at the dominant period of 30 s against to observed data. Epicenters are marked by beachballs in the topographic map, while solid yellow dots denote stations. Raypath colors match the corresponding stations next to the seismograms.

methods to evaluate resolution for an inverse problem, the checkerboard test is the most popular and relatively robust approach to estimating uncertainties in the linearized tomographic inversion with low computational costs, despite the fact that synthetic inversions, known to be called an “inversion crime”, may heavily overestimate the resolving power, potentially misleading even in linear inverse problems (Humphreys & Clayton, 1988; Igel, 2017; Lévêque et al., 1993). Here, the checkerboard test is computationally prohibitive for assessing 3-D FWI quality, which requires roughly the same amount of computational resources as the actual inversion. One of the main problems facing resolution analysis and uncertainty quantification in FWI is that seismic waveforms inherently depend nonlinearly on the Earth’s structure, meaning that the well-established machinery of linear inverse theory is no longer applicable (Backus & Gilbert, 1967; Tarantola, 2005). Generally, the nonlinear resolution analysis rests on (a) a quadratic approximation of the misfit functional in the vicinity of an optimal model, (b) an approximation of the Hessian built efficiently by gradient information from a set of perturbed models around the optimal model (Fichtner & Trampert, 2011a, 2011b). The inverse of the pre-conditioned Hessian can serve as a proxy of the posterior covariance from which space-dependent uncertainties and correlations between parameters and interparameter trade-offs can be conservatively extracted. The stochastic-gradient optimization scheme employed in this work, however, adds new complexity to the already complex nonlinear resolution analysis in the sense of non-identity Hessian information. To ameliorate this problem, we introduce a novel strategy to rigorously evaluate interparameter trade-offs between different physical parameters and the spatial resolution in the whole volume of interest by repairing the input 3-D Gaussian-sphere perturbations of the final model with a few L-BFGS iterations.

When synthetic waveforms can well fit the observed data and the inversion has reached convergence, input localized anomalies  $\delta m$  that perturbed the final model will be repaired or removed within the well-covered areas through several additional iterations. The difference between the final model and the reconstructed model can provide substantial information about the resolution length and trade-offs between different model parameters.

We perturbed the final model (*SinoScope 1.0*) by interleaved Gaussian spheres with  $\pm 8\%$  maximum amplitude of the vertically polarized shear wave velocity ( $V_{SV}$ ) for a specific depth and standard deviation  $\sigma$ , leaving other parameters unchanged. The horizontal grid spacing of the Gaussian spheres are 400 km (with  $\sigma = 40$  km at 20 km depth), 500 km (with  $\sigma = 50$  km at 300 km depth), and 600 km (with  $\sigma = 60$  km at 650 km depth). We adopt the parameter  $\mathbf{R}$  to evaluate the degree of repairment for the input perturbations quantitatively.

$$\mathbf{R} = \frac{\mathbf{m}_2 - \mathbf{m}_3}{\mathbf{m}_2 - \mathbf{m}_1} \quad \text{s. t. } \mathbf{m}_2 \neq \mathbf{m}_1 \quad (4)$$

where  $\mathbf{m}_1$ ,  $\mathbf{m}_2$ , and  $\mathbf{m}_3$  are the final model (*SinoScope 1.0*), the perturbed model, and the reconstructed model, respectively. When the input perturbation is completely removed,  $\mathbf{R}$  is equal to 1.0; by contrast, when the input perturbation fails to be repaired,  $\mathbf{R}$  is less than or equal to 0.0. We consider that the seismic structure can be well recovered when  $\mathbf{R}$  is  $\geq 0.4$  and  $\mathbf{R}$  is  $\leq 1.2$  at the corresponding grid node of the final model.

The conservative resolution length of each parameter of interest will be obtained with roughly 10 iterations, shown in Figure 10 and Figures S1–S5 in Supporting Information S1. Although additional iterations still have the potential to improve the amplitude recovery, it is legitimate to terminate the iteration for the computational reasons at this point. Gaussian anomalies are reasonably well removed within the crust and upper mantle, which is an expected result of the dominant position of the surface wave in the data set and the sensitivity distribution of the surface wave. At greater depths, our data set still has an ability to illuminate the Asian region very well because of the incorporation of the body wave. Furthermore, the trade-off with other model parameters mainly occurs as random noise near the surface and does not produce a significant anomaly at the disturbance location. The resolution analysis shows that we can quantitatively interpret the observational characteristics spanning from the western subduction zones of the Pacific Plate to the north of the Indo-Australian Plate.

## 5. Results and Discussion

We have applied the methods described in the above sections to our waveform data set for the radially anisotropic crust-mantle structure in the broad Asian region. The lateral averages of the horizontally and vertically polarized shear wave velocities ( $V_{SH}$  and  $V_{SV}$ ), density ( $\rho$ ), and radial shear wave anisotropy  $\xi = \frac{V_{SH} - V_{SV}}{V_S}$  of the final model compared against the initial model are presented in Figure 11, where  $V_S$  is the Voigt-Reuss-Hill average shear wave velocity, computed from SV and SH velocities as  $V_S = \sqrt{\frac{2V_{SV}^2 + V_{SH}^2}{3}}$  (Panning & Romanowicz, 2006). The average density does not change significantly from the initial model because the density is generally difficult to be constrained by seismic data within the period range of this study (e.g., Blom et al., 2017).

Since the early 2000s, many researchers have employed ambient noise, body wave, surface wave, and/or joint data sets to obtain more coherent and robust images of both compressional- and shear-wave velocities beneath the broad Asian region with superior data coverage and more solid theoretical foundations, ranging from local and regional (e.g., Chen et al., 2015; Han et al., 2021; Huang & Zhao, 2006; Hung et al., 2011; Lebedev & Nolet, 2003; Li & van der Hilst, 2010; Ma et al., 2019; Shen et al., 2016; Tao et al., 2018; Yao et al., 2006; Zheng et al., 2008) to global scale (e.g., Bozdağ et al., 2016; Koelemeijer et al., 2015; Lei et al., 2020; Li et al., 2008; Ritsema et al., 2011; Schaeffer & Lebedev, 2013; Zhao, 2004). However, damped least square tomographic models within ray theoretical or finite frequency physical frameworks can be locally biased toward lower or higher amplitudes in regions of poor data coverage, thus potentially causing physical misinterpretations (e.g., Nolet, 2008; Zoroli et al., 2017). For global-scale studies, strong smoothing has to be applied to balance imperfect data coverage, which will lead to the removal of short-wavelength structures that we do not expect to be resolvable with a given set of data, resulting in a relatively smooth Earth model. On balance, we present a comparison with a regional full-waveform tomographic model FWEA18 (Tao et al., 2018), which is a refined version of the continent-scale full-waveform tomographic model EARA2014 (Chen et al., 2015). Both *SinoScope 1.0* and FWEA18 image well-defined low-velocity and high-velocity anomaly patterns beneath East Asia (Figures S6–S9 in Supporting Information S1). As *SinoScope 1.0* is constructed with much denser data coverage and a novel stochastic-gradient optimization strategy, it captures sharper velocity contrasts across tectonic unit boundaries, stronger correlations of velocity anomalies with surface expressions, and well-confined narrow low-velocity asthenosphere and high-velocity slab features. Figure S10 in the Supporting Information S1 shows several waveform matches for observed data with synthetics obtained from *SinoScope 1.0* and FWEA18, and *SinoScope 1.0* can well fit the waveform evolution with distance, whereas FWEA18 does not. Both of the above provide evidence of a higher resolution in *SinoScope 1.0* than FWEA18.



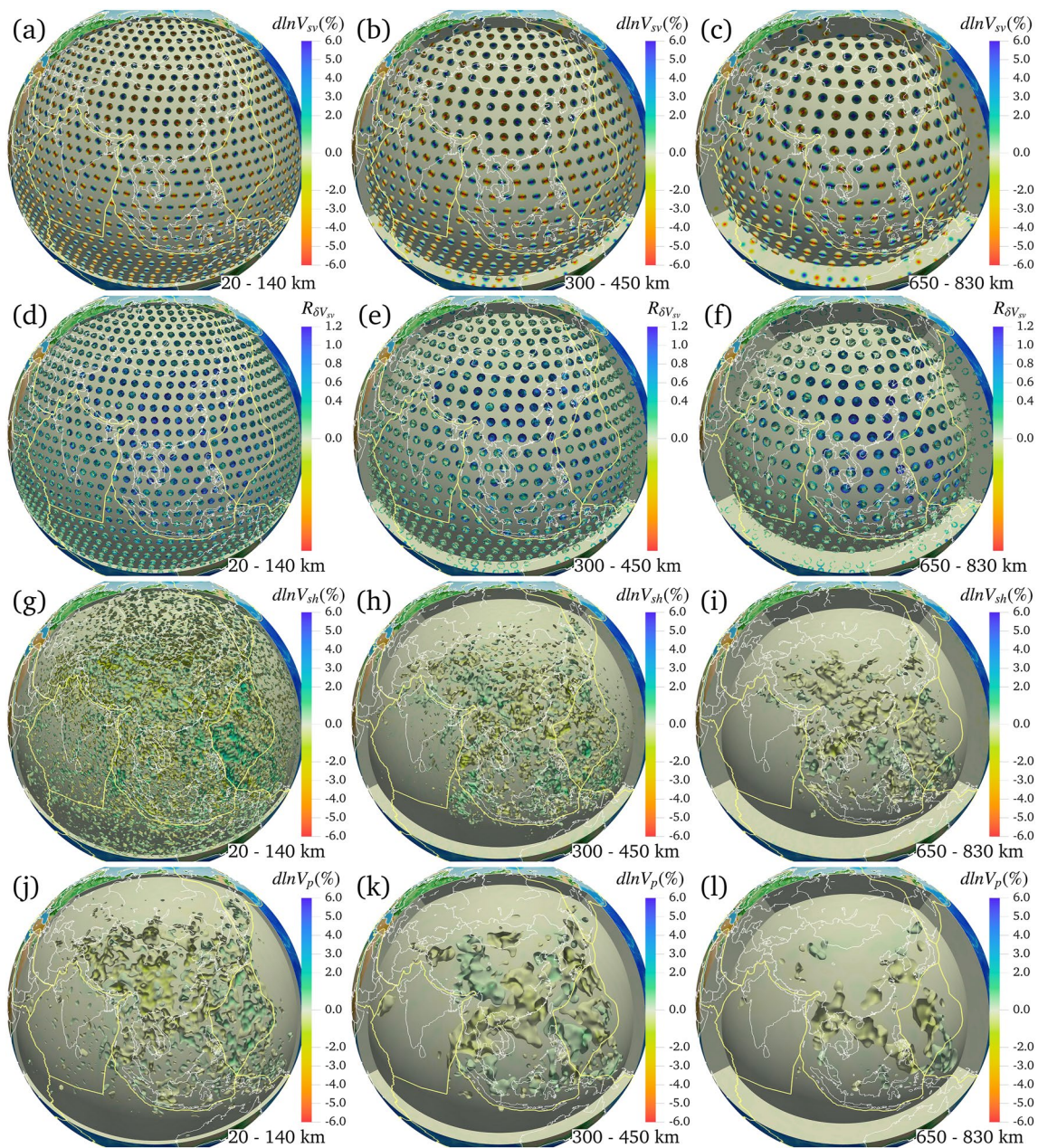


**Figure 10.** Resolution analysis and trade-offs estimates between model parameters based on iterative repairment experiments of random parametric perturbations. (a–c): 3-D visualizations of input  $\pm 8\%$  Gaussian  $V_{SV}$  perturbations ( $\delta V_{SV}$ ) at 20 km depth ( $\sigma = 40$  km), 300 km depth ( $\sigma = 50$  km), and 650 km depth ( $\sigma = 60$  km); (d–f): The degree of repairment for the input perturbations with respect to  $V_{SV}$ , which provides ample information about the seismic structure and length scale our data set can robustly resolve; (g–i): Difference between *SinoScope 1.0* and the reconstructed model with respect to  $V_{SH}$ , which represents the trade-offs between  $V_{SV}$  and  $V_{SH}$ ; (j–l): Difference between *SinoScope 1.0* and the reconstructed model with respect to  $V_p$ , which represents the trade-offs between  $V_{SV}$  and  $V_p$ .

The final tomographic model is presented in Figures 12–14 at constant depths, shown as the absolute isotropic S-wave velocities. High-resolution seismic images reveal significant lateral heterogeneities in the crust and mantle. This provides fruitful information about the depth extension of surface geological features and the influence and control of mantle dynamics upon lithospheric processes such as mountain building, seismogenesis, and volcanism. The radial anisotropy parameter  $\xi = (V_{SH} - V_{SV})/V_S$  is the relative seismic wave velocity difference between horizontally (SH) and vertically (SV) polarized shear waves, which can be treated as an important indicator of whether lithospheric deformation in the crust and mantle or mantle flow in the asthenosphere is dominant in either the horizontal direction (positive  $\xi$ ,  $V_{SH} > V_{SV}$ ) or the verti-



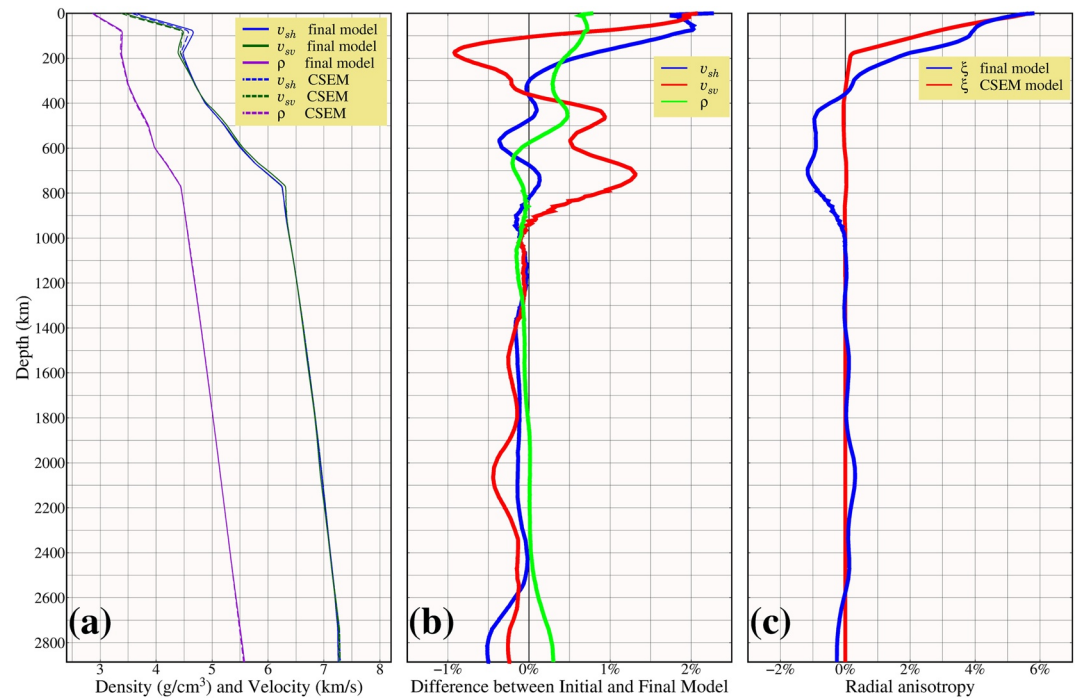


**Figure 11.** (a) Depth averages of the horizontally and vertically polarized shear wave velocities ( $V_{SH}$  and  $V_{SV}$ ) and mass density ( $\rho$ ) of the final model compared to the initial model Collaborative Seismic Earth Model (Fichtner et al., 2018). (b and c) Depth average of the magnitude of the relative difference between the initial and final models for model parameters ( $V_{SH}$ ,  $V_{SV}$ , and  $\rho$ ) and radial shear wave anisotropy ( $\xi$ ). The model has been updated considerably for all parameters from the surface down to the core-mantle boundary through multi-scale evolutionary inversions. Especially, average shear velocities change significantly from the initial model above 1,000 km, reflected in the corresponding depth-averaged anisotropy.

cal direction (negative  $\xi$ ,  $V_{SV} > V_{SH}$ ) (e.g., Fichtner et al., 2010; Zhu et al., 2017). The geologic/tectonic interpretation guided by seismic velocity and radial anisotropy is work in progress and will be presented in subsequent publications.

The model not only confirms well-established features but also exhibits sharper and more detailed shear wave velocity anomalies. Within the depth range of the lithosphere, the sharp transition from high-velocity to low-velocity anomalies clearly marks plate boundaries among the Eurasian Plate, Indo-Australian Plate, Philippine Sea Plate, Pacific Plate, and tectonic boundaries between the Tarim Basin and the Tibetan Plateau, the Sichuan Basin and the Chuandian Block, and the North China Block and the South China Block (Figure 12). The large-scale low-velocity anomalies beneath the Tibetan Plateau are roughly bounded by the Tarim Basin in the northwest, Ordos and Sichuan Basins in the east, the Alxa Block in the north, and the north margin of the Indian Plate in the south (Figure 12; e.g., Han et al., 2021; Shen et al., 2016). The Indian Plate has subducted down to 250–300 km depth underneath the Tibetan Plateau, with the northern frontal edge of the Indian slab reaching the Songpan Ganzi Fold Belt (Figures 12 and 13). The western Pacific slab, imaged as a high-velocity zone, is subducting beneath the Eurasian Plate from Kuril trench, Japan trench, Izu-Bonin trench, and Mariana trench down to the deep mantle (Figures 12 and 13; e.g., Chen et al., 2015; Huang & Zhao, 2006; Li & van der Hilst, 2010; Li et al., 2008; Tao et al., 2018). The Philippine Sea and Caroline plates are characterized by conspicuous high-velocity anomalies in the lithosphere to a depth of  $\sim 90$  km (Figure 12), underlain by the low-velocity zone (generally referred to as the asthenosphere; e.g., Barrell, 1914) in the upper mantle (Figures 12 and 13).

Below the base of the lithosphere, our results exhibit notable widespread asthenosphere with a thickness of  $\sim 100$  km in East and Southeast Asia, bounded by subduction trenches (Kurile, Japan, Ryukyu, Philippine, Timor, Java, Sumatra, Andaman, and Arakan), the Ordos Block and Sichuan Basin (Figures 12 and 13). Under the Stanovoy Range and north part of Northeast China, the low-velocity anomalies are still prominent down to the top of the mantle transition zone (MTZ; Figures 12 and 13). The strong low-velocity bodies correlated

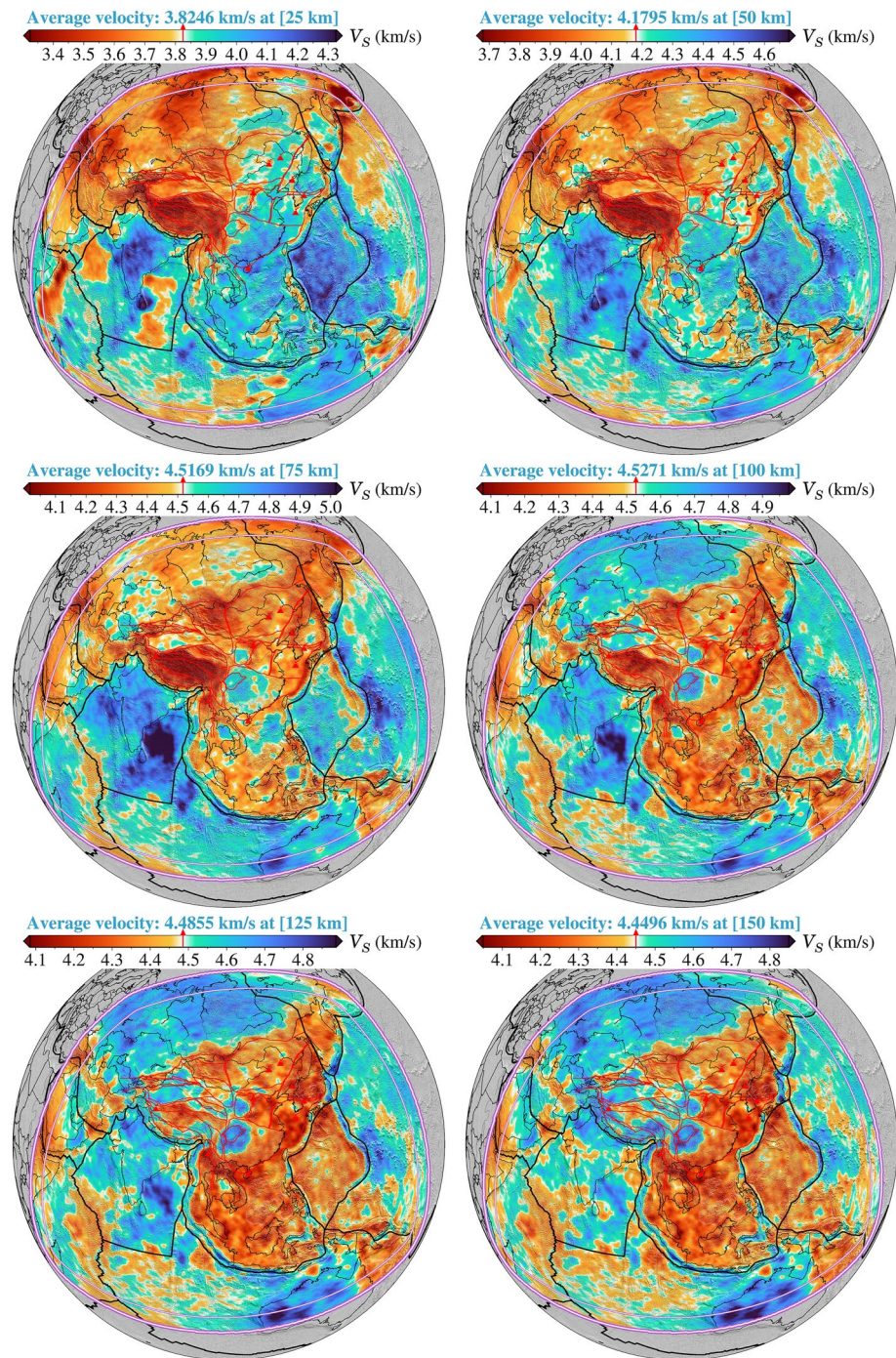


**Figure 12.** Horizontal slices through the final tomographic model showing the absolute isotropic  $V_S$  for the lithosphere at various depths. The depth of each layer is shown on the top of each map.  $V_S$  is the Voigt-Reuss-Hill average shear wave velocity. The thick white outer line marks the edge of the computational domain where we run all kinds of simulations and inversion procedures, and the thin white inner line marks the start of the absorbing boundary region. Within the buffer zone between the outer and inner model boundaries, wave propagation energy will be absorbed that would otherwise result in artificial reflections. The red triangles denote active intraplate volcanoes. The other labeling is the same as that in Figure 1. Please note that different color scales are used for different depth levels.

with the Altay-Sayan Mountain Range continuously extend from the crust to the uppermost mantle (Figures 12 and 13). The active intraplate volcanic areas in East Asia (such as Wudalianchi, Arxan, Jingpo Lake, Changbai, Datong, Ulleung, Jeju, and Tengchong) are underlain by significant low-velocity anomalies in the upper mantle (Figures 12 and 13). Beneath the Indo-Australian Plate, we observe distinct low-velocity anomalies from a depth



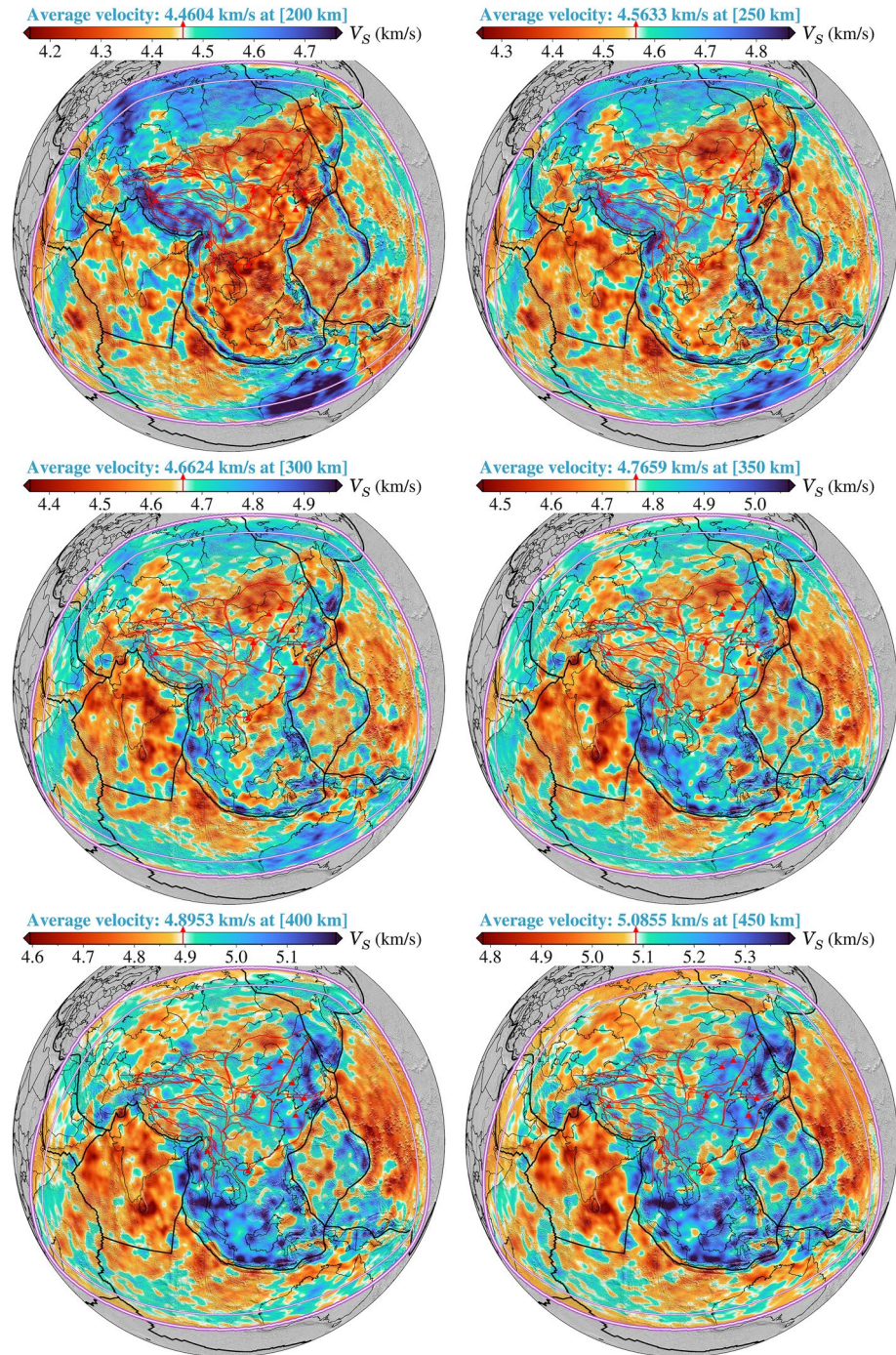


**Figure 13.** Horizontal slices through the final tomographic model showing the absolute isotropic  $V_S$  for the lowermost upper mantle, mantle transition zone, and uppermost lower mantle at various depths. The depth of each layer is shown on the top of each map. The other labeling is the same as that in Figure 12. Please note that different color scales are used for different depth levels.

of ~200 km to the bottom of the MTZ, continuously extending northward below western China from the lower MTZ to the top of the lower mantle (Figures 13 and 14).

Southeast Asia, as one of the most complex tectonic regions on Earth, is currently surrounded by strongly curved subduction zones. One dominant feature in our images is the high-velocity zones around Southeast Asia (Figures 12 and 13), which generally represent the subducting slabs, such as the Burma slab under Southeast Tibet,



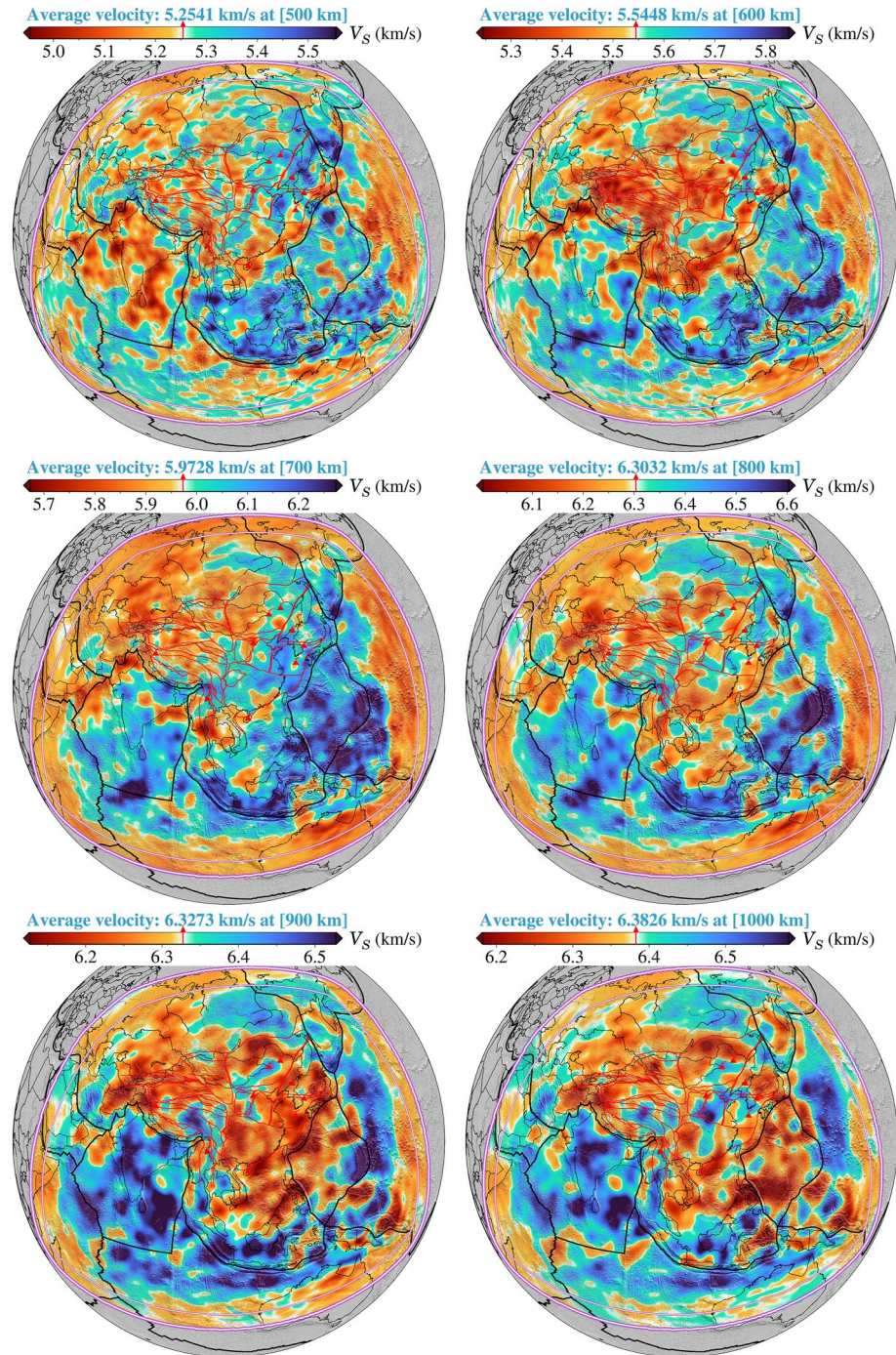


**Figure 14.** Horizontal slices through the final tomographic model showing the absolute isotropic  $V_S$  for the lower mantle down to 1,000 km depth at various depths. The depth of each layer is shown on the top of each map. The other labeling is the same as that in Figure 12. Please note that different color scales are used for different depth levels.

the Australian slab under Sumatra and Java, the Philippine Sea slab under the Philippines, and the Molucca Sea slabs under the eastern Indonesia. Our results reveal clearly sub-horizontal high-velocity anomalies in and around the MTZ (Figure 13), which have been well identified from previous tomographic studies but there has been little agreement on their origin (e.g., Hall & Spakman, 2015; Obayashi et al., 2013). Narrow east-northeast striking high-velocity anomalies appear from the top of the MTZ down to a depth of 900 km beneath the Caroline Plate (Figures 13 and 14), suggesting that ancient continental or oceanic lithosphere resides inside the MTZ, penetrates

the 660-km discontinuity and sinks into the lower mantle, possibly corresponding to different episodes of the slab subduction. Significant high-velocity anomalies are visible in the uppermost lower mantle beneath the north of the Indo-Australian Plate (Figure 14), which may represent fragments of the late Mesozoic Tethyan slab subducted before the India-Eurasia collision (e.g., Nerlich et al., 2016).

## 6. Conclusions

We conducted a 3-D FWI for the crust-mantle structure beneath China and adjacent regions based on numerical forward and adjoint simulations of anelastic seismic wave propagation with the shortest period of 30 s. New model *SinoScope 1.0* reveals high-velocity anomalies in the upper mantle beneath major subduction zones and three stable blocks (Ordos, Sichuan, and Tarim basins) and low-velocity anomalies beneath Holocene volcanoes, back-arc regions of ongoing subductions, and India-Eurasia collision zone, which are generally viewed as well-established features of the broad Asian region (e.g., Chen et al., 2015, 2017; Huang & Zhao, 2006; Li & van der Hilst, 2010; Tao et al., 2018). It can further advance our understanding of the tectonic evolution, plate subductions, and mantle dynamics in the broad Asian region. Furthermore, *SinoScope 1.0* will be employed to estimate the present-day mantle heterogeneity state to retrodict the history of mantle flow and dynamic topography in the subsequent works through the adjoint method introduced by Bunge et al. (2003), building upon our previous works presented by Colli et al. (2018) and Ghelichkhan et al. (2021).

The ~0.53 million 60-min three-component seismograms from 410 earthquakes recorded at 2,427 seismic stations were employed in three successively broadened period bands of 70–120 s, 50–120 s, and 30–120 s, resulting in the assimilation of more than 10 million time windows throughout the inversion's three stages. *SinoScope 1.0* is simultaneously constrained by three-component long-period surface waves and short-period body waves and updated by the non-linear minimization of time-frequency domain phase misfits, bringing out numerous small-scale features not observed in previous tomography models. To judge the quality of the model, we performed a validation test with a few earthquakes not used in the construction of the model to demonstrate that it provides significant improvements in phase and amplitude fits compared to the initial model. In addition, we conducted a detailed resolution analysis before interpreting the final model and its features.

Given the rapidly growing volume of seismological waveform data released by various international seismic networks, advances in computational power and numerical optimization routines have enabled the possibility of tackling finer-scale and more complex tomography problems in the coming future. This will undoubtedly drive more work to produce the second-generation full-waveform tomographic model (*SinoScope 2.0*), especially motivated by the deployment of a large-scale broadband seismic array (ChinArray, <http://www.chinarraydmc.cn>), which densely covers the entire mainland China and is spaced ~35–40 km apart on average. Evident future work needs to assimilate the quick-growing earthquake database recorded by a few seismic networks not available now, for example, ChinArray, Russian Seismic Network, Mongolian Seismic Network, Indian Seismic Network, Indonesian Seismic Network, Pacific Array (<http://eri-ndc.eri.u-tokyo.ac.jp/PacificArray/>), and reduce the shortest simulation period further from 30 to 10 s, or lower in order to more sufficiently constrain physical properties of the Earth's interior and further improve resolution without producing local artifacts.

## Data Availability Statement

The free software GMT (Wessel et al., 2013) is used for making most of the figures. The 3-D renderings of the visualizations (Figures 7 and 10) are generated using ParaView software (Ayachit, 2015). Source parameters adopted in the wavefield simulations were extracted from the GCMT catalog (<https://www.globalcmt.org/CMTsearch.html>). The anisotropic seismic tomography model presented in this study (which we call *SinoScope 1.0*) and the waveform data for this research are available on the Zenodo repository: <https://doi.org/10.5281/zenodo.6597380>.

## References

- Afanasiev, M., Boehm, C., van Driel, M., Krischer, L., Rietmann, M., May, D. A., et al. (2019). Modular and flexible spectral-element waveform modelling in two and three dimensions. *Geophysical Journal International*, 216(3), 1675–1692. <https://doi.org/10.1093/gji/ggy469>
- Afanasiev, M., Peter, D., Sager, K., Simutè, S., Ermert, L., Krischer, L., & Fichtner, A. (2016). Foundations for a multiscale collaborative Earth model. *Geophysical Journal International*, 204(1), 39–58. <https://doi.org/10.1093/gji/ggv439>

## Acknowledgments

The authors thank the Data Management Center of China National Seismic Network (<http://www.seisdmc.ac.cn>), the Full Range Seismograph Network of Japan (F-net, <http://www.fnet.bosai.go.jp>), the National Seismograph Network of South Korea and the IRIS Data Management Center (<http://ds.iris.edu/ds/nodes/dmc/>) for providing the high-quality waveform data used in this study. Specifically, the authors gratefully acknowledge the Gauss Center for Supercomputing e.V. ([www.gauss-centre.eu](http://www.gauss-centre.eu)) for funding this project by providing computing time on the GCS Supercomputer SuperMUC-NG at Leibniz Supercomputing Center ([www.lrz.de](http://www.lrz.de)) and support from the Swiss National Supercomputing Center (SCSC) in the form of computing time grants s1040. J. Ma and T. Liu acknowledge the financial support from the China Scholarship Council. S. Thrastarson and D. -P. van Herwaarden were supported by the European Unions Horizon 2020 research and innovation programme through an European Research Council Starting Grant (The Collaborative Seismic Earth Model, Grant No. 714069). Y. Tian was supported by the grant from the National Natural Science Foundation of China (Grant No. 41874049). S.-J. Chang was supported by the Korea Meteorological Administration Research and Development Program under Grant KMI 2022-00810, by the National Research Foundation of Korea (NRF) grant funded by the Korean government (MSIT) (2019R1A2C208506111), and by Basic Science Research Program through the NRF funded by the Ministry of Education (No. 2019R1A6A1A03033167). The authors would also like to thank Christian Boehm, Lion Krischer, and Michael Afanasiev for fruitful discussions. Many thanks also to Jens Oeser for building an excellent computing infrastructure at the Institute of Geophysics at LMU München, without which it is impossible to perform one single numerical simulation. The authors are very grateful to Michael Bostock (the Editor), Jiaqi Li, and an anonymous reviewer for their constructive comments and suggestions that improved the manuscript. Open Access funding enabled and organized by Projekt DEAL.



- Aki, K., Christofferson, A., & Husebye, E. S. (1977). Determination of the three-dimensional seismic structure of the lithosphere. *Journal of Geophysical Research*, 82(2), 277–296. <https://doi.org/10.1029/jb082i002p00277>
- Aki, K., & Lee, W. H. K. (1976). Determination of three-dimensional velocity anomalies under a seismic array using first *p* arrival times from local earthquakes: 1. A homogeneous initial model. *Journal of Geophysical Research*, 81(23), 4381–4399. <https://doi.org/10.1029/jb081i023p04381>
- Ayachit, U. (2015). *The paraview guide: A parallel visualization application*. Kitware, Inc.
- Backus, G. E., & Gilbert, J. F. (1967). Numerical applications of a formalism for geophysical inverse problems. *Geophysical Journal International*, 13(1–3), 247–276. <https://doi.org/10.1111/j.1365-246X.1967.tb02159.x>
- Barrell, J. (1914). The strength of the Earth's crust. *The Journal of Geology*, 22(7), 655–683. <https://doi.org/10.1086/622181>
- Bird, P. (2003). An updated digital model of plate boundaries. *Geochemistry, Geophysics, Geosystems*, 4(3). <https://doi.org/10.1029/2001gc000252>
- Blom, N., Boehm, C., & Fichtner, A. (2017). Synthetic inversions for density using seismic and gravity data. *Geophysical Journal International*, 209(2), 1204–1220. <https://doi.org/10.1093/gji/ggx076>
- Boehm, C., Korta Martiartu, N., Vinard, N., Jovanović Balic, I., & Fichtner, A. (2018). Time-domain spectral-element ultrasound waveform tomography using a stochastic quasi-Newton method. In *Medical imaging 2018: Ultrasonic imaging and tomography* (Vol. 10580, p. 105800H). <https://doi.org/10.1117/12.2293299>
- Bozdag, E., Peter, D., Lefebvre, M., Komatitsch, D., Tromp, J., Hill, J., et al. (2016). Global adjoint tomography: First-generation model. *Geophysical Journal International*, 207(3), 1739–1766. <https://doi.org/10.1093/gji/ggw356>
- Bunge, H.-P., Hagelberg, C. R., & Travis, B. J. (2003). Mantle circulation models with variational data assimilation: Inferring past mantle flow and structure from plate motion histories and seismic tomography. *Geophysical Journal International*, 152(2), 280–301. <https://doi.org/10.1046/j.1365-246X.2003.01823.x>
- Bunks, C., Saleck, F. M., Zaleski, S., & Chavent, G. (1995). Multiscale seismic waveform inversion. *Geophysics*, 60(5), 1457–1473. <https://doi.org/10.1190/1.1443880>
- Chen, M., Niu, F., Liu, Q., Tromp, J., & Zheng, X. (2015). Multiparameter adjoint tomography of the crust and upper mantle beneath East Asia: 1. Model construction and comparisons. *Journal of Geophysical Research: Solid Earth*, 120, 1762–1786. <https://doi.org/10.1002/2014jb011638>
- Chen, M., Niu, F., Tromp, J., Lenardic, A., Lee, C.-T. A., Cao, W., & Ribeiro, J. (2017). Lithospheric foundering and underthrusting imaged beneath Tibet. *Nature Communications*, 8(1), 1–10. <https://doi.org/10.1038/ncomms15659>
- Colli, L., Fichtner, A., & Bunge, H.-P. (2013). Full waveform tomography of the upper mantle in the south Atlantic region: Imaging a westward fluxing shallow asthenosphere? *Tectonophysics*, 604, 26–40. (Progress in understanding the South Atlantic margins). <https://doi.org/10.1016/j.tecto.2013.06.015>
- Colli, L., Ghelichkhan, S., Bunge, H.-P., & Oeser, J. (2018). Retrodictions of Mid Paleogene mantle flow and dynamic topography in the Atlantic region from compressible high resolution adjoint mantle convection models: Sensitivity to deep mantle viscosity and tomographic input model. *Gondwana Research*, 53, 252–272. <https://doi.org/10.1016/j.gr.2017.04.027>
- Conn, A. R., Gould, N. I. M., & Toint, P. L. (2000). *Trust region methods*. Society for Industrial and Applied Mathematics. Retrieved from <https://epubs.siam.org/doi/abs/10.1137/1.9780898719857>
- Dahlen, F. A., Hung, S.-H., & Nolet, G. (2000). Fréchet kernels for finite-frequency traveltimes—I. Theory. *Geophysical Journal International*, 141(1), 157–174. <https://doi.org/10.1046/j.1365-246X.2000.00070.x>
- DeMets, C., Gordon, R. G., Argus, D. F., & Stein, S. (1994). Effect of recent revisions to the geomagnetic reversal time scale on estimates of current plate motions. *Geophysical Research Letters*, 21(20), 2191–2194. <https://doi.org/10.1029/94gl02118>
- Dziewonski, A. M., & Anderson, D. L. (1981). Preliminary reference Earth model. *Physics of the Earth and Planetary Interiors*, 25(4), 297–356. [https://doi.org/10.1016/0031-9201\(81\)90046-7](https://doi.org/10.1016/0031-9201(81)90046-7)
- Dziewonski, A. M., Hager, B. H., & O'Connell, R. J. (1977). Large-scale heterogeneities in the lower mantle. *Journal of Geophysical Research*, 82(2), 239–255. <https://doi.org/10.1029/jb082i002p00239>
- Ekström, G., Nettles, M., & Dziewoński, A. (2012). The global CMT project 2004–2010: Centroid-moment tensors for 13, 017 earthquakes. *Physics of the Earth and Planetary Interiors*, 200–201, 1–9. <https://doi.org/10.1016/j.pepi.2012.04.002>
- Fichtner, A. (2011). *Full seismic waveform modelling and inversion*. Springer. <https://doi.org/10.1007/978-3-642-15807-0>
- Fichtner, A., Bunge, H.-P., & Igel, H. (2006). The adjoint method in seismology: I. Theory. *Physics of the Earth and Planetary Interiors*, 157(1), 86–104. <https://doi.org/10.1016/j.pepi.2006.03.016>
- Fichtner, A., Kennett, B. L. N., Igel, H., & Bunge, H.-P. (2008). Theoretical background for continental-and global-scale full-waveform inversion in the time–frequency domain. *Geophysical Journal International*, 175(2), 665–685. <https://doi.org/10.1111/j.1365-246X.2008.03923.x>
- Fichtner, A., Kennett, B. L. N., Igel, H., & Bunge, H.-P. (2009). Full seismic waveform tomography for upper-mantle structure in the Australasian region using adjoint methods. *Geophysical Journal International*, 179(3), 1703–1725. <https://doi.org/10.1111/j.1365-246X.2009.04368.x>
- Fichtner, A., Kennett, B. L. N., Igel, H., & Bunge, H.-P. (2010). Full waveform tomography for radially anisotropic structure: New insights into present and past states of the Australasian upper mantle. *Earth and Planetary Science Letters*, 290(3), 270–280. <https://doi.org/10.1016/j.epsl.2009.12.003>
- Fichtner, A., & Trampert, J. (2011a). Hessian kernels of seismic data functionals based upon adjoint techniques. *Geophysical Journal International*, 185(2), 775–798. <https://doi.org/10.1111/j.1365-246X.2011.04966.x>
- Fichtner, A., & Trampert, J. (2011b). Resolution analysis in full waveform inversion. *Geophysical Journal International*, 187(3), 1604–1624. <https://doi.org/10.1111/j.1365-246X.2011.05218.x>
- Fichtner, A., van Herwaarden, D.-P., Afanasiev, M., Simuté, S., Krischer, L., Çubuk Sabuncu, Y., et al. (2018). The collaborative seismic Earth model: Generation 1. *Geophysical Research Letters*, 45(9), 4007–4016. <https://doi.org/10.1029/2018gl077338>
- French, S. W., & Romanowicz, B. A. (2014). Whole-mantle radially anisotropic shear velocity structure from spectral-element waveform tomography. *Geophysical Journal International*, 199(3), 1303–1327. <https://doi.org/10.1093/gji/ggu334>
- Ghelichkhan, S., Bunge, H.-P., & Oeser, J. (2021). Global mantle flow retrodictions for the early Cenozoic using an adjoint method: Evolving dynamic topographies, deep mantle structures, flow trajectories and sublithospheric stresses. *Geophysical Journal International*, 226(2), 1432–1460. <https://doi.org/10.1093/gji/ggab108>
- Gokhberg, A., & Fichtner, A. (2016). Full-waveform inversion on heterogeneous HPC systems. *Computers & Geosciences*, 89, 260–268. <https://doi.org/10.1016/j.cageo.2015.12.013>
- Grand, S., van der Hilst, R., & Widiyantoro, S. (1997). Global seismic tomography: A snapshot of convection in the Earth. *Geological Society of America TODAY*, 7, 1–7.
- Hall, R. (2011). Australia–SE Asia collision: Plate tectonics and crustal flow. In *The SE Asian gateway: History and tectonics* (Vol. 355, pp. 75–109). Geological Society of London Special Publications. <https://doi.org/10.1144/SP355.5>



- Hall, R., & Spakman, W. (2015). Mantle structure and tectonic history of SE Asia. *Tectonophysics*, 658, 14–45. <https://doi.org/10.1016/j.tecto.2015.07.003>
- Han, S., Zhang, H., Xin, H., Shen, W., & Yao, H. (2021). USTClitho2.0: Updated unified seismic tomography models for continental China lithosphere from joint inversion of body-wave arrival times and surface-wave dispersion data. *Seismological Research Letters*, 93(1), 201–215. <https://doi.org/10.1785/0220210122>
- Hayes, G. P., Moore, G. L., Portner, D. E., Hearne, M., Flamme, H., Furtney, M., & Smoczyk, G. M. (2018). Slab2, a comprehensive subduction zone geometry model. *Science*, 362(6410), 58–61. <https://doi.org/10.1126/science.aat4723>
- Hosseini, K., Sigloch, K., Tsekhmistrenko, M., Zaheri, A., Nissen-Meyer, T., & Igel, H. (2020). Global mantle structure from multifrequency tomography using P, PP, and P-diffracted waves. *Geophysical Journal International*, 220(1), 96–141. <https://doi.org/10.1093/gji/ggz394>
- Huang, J., & Zhao, D. (2006). High-resolution mantle tomography of China and surrounding regions. *Journal of Geophysical Research*, 111, B09305. <https://doi.org/10.1029/2005jb004066>
- Humphreys, E., & Clayton, R. W. (1988). Adaptation of back projection tomography to seismic travel time problems. *Journal of Geophysical Research*, 93(B2), 1073–1085. <https://doi.org/10.1029/jb093ib02p01073>
- Hung, S.-H., Chen, W.-P., & Chiao, L.-Y. (2011). A data-adaptive, multiscale approach of finite-frequency, traveltimes tomography with special reference to P and S wave data from central Tibet. *Journal of Geophysical Research*, 116, B06307. <https://doi.org/10.1029/2010JB008190>
- Hung, S.-H., Dahlen, F., & Nolet, G. (2000). Fréchet kernels for finite-frequency traveltimes—II. Examples. *Geophysical Journal International*, 141(1), 175–203. <https://doi.org/10.1046/j.1365-246x.2000.00072.x>
- Igel, H. (2017). *Computational seismology: A practical introduction*. Oxford University Press.
- Jolivet, L., Faccenna, C., Becker, T., Tesauro, M., Sternai, P., & Bouilhol, P. (2018). Mantle flow and deforming continents: From India-Asia convergence to Pacific subduction. *Tectonics*, 37(9), 2887–2914. <https://doi.org/10.1029/2018tc005036>
- Kennett, B. L. N., & Fichtner, A. (2020). *Exploiting seismic waveforms: Correlation, heterogeneity, and inversion*. Cambridge University Press. <https://doi.org/10.1017/9781108903035>
- Koelenmeijer, P., Ritsema, J., Deuss, A., & van Heijst, H.-J. (2015). SP12RTS: A degree-12 model of shear-and compressional-wave velocity for Earth's mantle. *Geophysical Journal International*, 204(2), 1024–1039. <https://doi.org/10.1093/gji/ggv481>
- Komatitsch, D., & Tromp, J. (2002a). Spectral-element simulations of global seismic wave propagation—I. Validation. *Geophysical Journal International*, 149(2), 390–412. <https://doi.org/10.1046/j.1365-246x.2002.01653.x>
- Komatitsch, D., & Tromp, J. (2002b). Spectral-element simulations of global seismic wave propagation—II. Three-dimensional models, oceans, rotation, and self-gravitation. *Geophysical Journal International*, 150(1), 303–318. <https://doi.org/10.1046/j.1365-246x.2002.01716.x>
- Kreemer, C., Blewitt, G., & Klein, E. C. (2014). A geodetic plate motion and global strain rate model. *Geochemistry, Geophysics, Geosystems*, 15(10), 3849–3889. <https://doi.org/10.1002/2014gc005407>
- Krischer, L., Fichtner, A., Boehm, C., & Igel, H. (2018). Automated large-scale full seismic waveform inversion for North America and the North Atlantic. *Journal of Geophysical Research: Solid Earth*, 123, 5902–5928. <https://doi.org/10.1029/2017jb015289>
- Krischer, L., Megies, T., Barsch, R., Beyreuther, M., Lecocq, T., Caudron, C., & Wassermann, J. (2015). ObsPy: A bridge for seismology into the scientific python ecosystem. *Computational Science & Discovery*, 8(1), 014003. <https://doi.org/10.1088/1749-4699/8/1/014003>
- Krischer, L., Smith, J., Lei, W., Lefebvre, M., Ruan, Y., de Andrade, E. S., et al. (2016). An adaptable seismic data format. *Geophysical Journal International*, 207(2), 1003–1011. <https://doi.org/10.1093/gji/ggw319>
- Kristeková, M., Kristek, J., & Moczo, P. (2009). Time-frequency misfit and goodness-of-fit criteria for quantitative comparison of time signals. *Geophysical Journal International*, 178(2), 813–825. <https://doi.org/10.1111/j.1365-246x.2009.04177.x>
- Kristeková, M., Kristek, J., Moczo, P., & Day, S. M. (2006). Misfit criteria for quantitative comparison of seismograms. *Bulletin of the Seismological Society of America*, 96(5), 1836–1850. <https://doi.org/10.1785/0120060012>
- Lebedev, S., & Nolet, G. (2003). Upper mantle beneath Southeast Asia from s velocity tomography. *Journal of Geophysical Research*, 108, 2048. <https://doi.org/10.1029/2000jb000073>
- Lei, W., Ruan, Y., Bozdağ, E., Peter, D., Lefebvre, M., Komatitsch, D., et al. (2020). Global adjoint tomography—Model GLAD-M25. *Geophysical Journal International*, 223(1), 1–21. <https://doi.org/10.1093/gji/ggaa253>
- Lekić, V., & Romanowicz, B. (2011). Inferring upper-mantle structure by full waveform tomography with the spectral element method. *Geophysical Journal International*, 185(2), 799–831. <https://doi.org/10.1111/j.1365-246x.2011.04969.x>
- Lévéque, J.-J., Rivera, L., & Wittlinger, G. (1993). On the use of the checker-board test to assess the resolution of tomographic inversions. *Geophysical Journal International*, 115(1), 313–318. <https://doi.org/10.1111/j.1365-246x.1993.tb05605.x>
- Li, C., & van der Hilst, R. D. (2010). Structure of the upper mantle and transition zone beneath Southeast Asia from traveltimes tomography. *Journal of Geophysical Research*, 115, B07308. <https://doi.org/10.1029/2009jb006882>
- Li, C., van der Hilst, R. D., Engdahl, E. R., & Burdick, S. (2008). A new global model for P wave speed variations in Earth's mantle. *Geochemistry, Geophysics, Geosystems*, 9(5), Q05018. <https://doi.org/10.1029/2007gc001806>
- Liu, D. C., & Nocedal, J. (1989). On the limited memory BFGS method for large scale optimization. *Mathematical Programming*, 45(1), 503–528. <https://doi.org/10.1007/bf01589116>
- Ma, J., Thrastarson, S., van Herwaarden, D.-P., Fichtner, A., & Bunge, H.-P. (2020). Multiscale seismic full-waveform tomography of the crust and mantle beneath China and adjacent regions. In *Egu general assembly conference abstracts* (p. 2967). <https://doi.org/10.5194/egusphere-egu2020-2967>
- Ma, J., Tian, Y., Zhao, D., Liu, C., & Liu, T. (2019). Mantle dynamics of western Pacific and East Asia: New insights from P wave anisotropic tomography. *Geochemistry, Geophysics, Geosystems*, 20(7), 3628–3658. <https://doi.org/10.1029/2019gc008373>
- Maggi, A., Tape, C., Chen, M., Chao, D., & Tromp, J. (2009). An automated time-window selection algorithm for seismic tomography. *Geophysical Journal International*, 178(1), 257–281. <https://doi.org/10.1111/j.1365-246x.2009.04099.x>
- Matharu, G., & Sacchi, M. (2019). A subsampled truncated-Newton method for multiparameter full-waveform inversion. *Geophysics*, 84(3), R333–R340. <https://doi.org/10.1190/geo2018-0624.1>
- Megies, T., Beyreuther, M., Barsch, R., Krischer, L., & Wassermann, J. (2011). ObsPy – What can it do for data centers and observatories? *Istituto Nazionale di Geofisica e Vulcanologia. INGV*, 54(1).
- Meier, U., Curtis, A., & Trampert, J. (2007a). Fully nonlinear inversion of fundamental mode surface waves for a global crustal model. *Geophysical Research Letters*, 34(16), 1–6. <https://doi.org/10.1029/2007gl030989>
- Meier, U., Curtis, A., & Trampert, J. (2007b). Global crustal thickness from neural network inversion of surface wave data. *Geophysical Journal International*, 169(2), 706–722. <https://doi.org/10.1111/j.1365-246x.2007.03373.x>
- Mitchell, D. P. (1991). Spectrally optimal sampling for distribution ray tracing. *Association for Computing Machinery (ACM)*, 25(4), 157–164. <https://doi.org/10.1145/127719.122736>

- Montelli, R., Nolet, G., Dahlen, F. A., Masters, G., Engdahl, E. R., & Hung, S.-H. (2004). Finite-frequency tomography reveals a variety of plumes in the mantle. *Science*, 303(5656), 338–343. <https://doi.org/10.1126/science.1092485>
- Nerlich, R., Colli, L., Ghelichkhan, S., Schubert, B., & Bunge, H.-P. (2016). Constraining central Neo-Tethys ocean reconstructions with mantle convection models. *Geophysical Research Letters*, 43(18), 9595–9603. <https://doi.org/10.1002/2016gl070524>
- Nocedal, J., & Wright, S. J. (1999). *Numerical optimization*. Springer.
- Nolet, G. (2008). A breviary of seismic tomography.
- Obayashi, M., Yoshimitsu, J., Nolet, G., Fukao, Y., Shiobara, H., Sugioka, H., et al. (2013). Finite frequency whole mantle P wave tomography: Improvement of subducted slab images. *Geophysical Research Letters*, 40(21), 5652–5657. <https://doi.org/10.1002/2013gl057401>
- Panning, M., & Romanowicz, B. (2006). A three-dimensional radially anisotropic model of shear velocity in the whole mantle. *Geophysical Journal International*, 167(1), 361–379. <https://doi.org/10.1111/j.1365-246x.2006.03100.x>
- Ritsema, J., Deuss, A., van Heijst, H. J., & Woodhouse, J. H. (2011). S40RTS: A degree-40 shear-velocity model for the mantle from new Rayleigh wave dispersion, teleseismic traveltime and normal-mode splitting function measurements. *Geophysical Journal International*, 184(3), 1223–1236. <https://doi.org/10.1111/j.1365-246x.2010.04884.x>
- Ritsema, J., & van Heijst, H.-J. (2002). Constraints on the correlation of P- and S-wave velocity heterogeneity in the mantle from P, PP, PPP, and PKPab traveltimes. *Geophysical Journal International*, 149(2), 482–489. <https://doi.org/10.1046/j.1365-246x.2002.01631.x>
- Ritsema, J., van Heijst, H. J., & Woodhouse, J. H. (1999). Complex shear wave velocity structure imaged beneath Africa and Iceland. *Science*, 286(5446), 1925–1928. <https://doi.org/10.1126/science.286.5446.1925>
- Schaeffer, A. J., & Lebedev, S. (2013). Global shear speed structure of the upper mantle and transition zone. *Geophysical Journal International*, 194(1), 417–449. <https://doi.org/10.1093/gji/ggt095>
- Seton, M., Müller, R. D., Zahirovic, S., Williams, S., Wright, N. M., Cannon, J., et al. (2020). A global data set of present-day oceanic crustal age and seafloor spreading parameters. *Geochemistry, Geophysics, Geosystems*, 21(10), e2020GC009214. <https://doi.org/10.1029/2020gc009214>
- Shen, W., Ritzwoller, M. H., Kang, D., Kim, Y., Lin, F.-C., Ning, J., et al. (2016). A seismic reference model for the crust and uppermost mantle beneath China from surface wave dispersion. *Geophysical Journal International*, 206(2), 954–979. <https://doi.org/10.1093/gji/ggw175>
- Simuté, S., Steptoe, H., Cobden, L., Gokhberg, A., & Fichtner, A. (2016). Full-waveform inversion of the Japanese islands region. *Journal of Geophysical Research: Solid Earth*, 121, 3722–3741. <https://doi.org/10.1002/2016jb02802>
- Tao, K., Grand, S. P., & Niu, F. (2018). Seismic structure of the upper mantle beneath eastern Asia from full waveform seismic tomography. *Geochemistry, Geophysics, Geosystems*, 19(8), 2732–2763. <https://doi.org/10.1029/2018gc007460>
- Tape, C., Liu, Q., Maggi, A., & Tromp, J. (2009). Adjoint tomography of the southern California crust. *Science*, 325(5943), 988–992. <https://doi.org/10.1126/science.1175298>
- Tape, C., Liu, Q., Maggi, A., & Tromp, J. (2010). Seismic tomography of the southern California crust based on spectral-element and adjoint methods. *Geophysical Journal International*, 180(1), 433–462. <https://doi.org/10.1111/j.1365-246x.2009.04429.x>
- Tapponnier, P., Peltzer, G., Le Dain, A. Y., Armijo, R., & Cobbold, P. (1982). Propagating extrusion tectonics in Asia: New insights from simple experiments with plasticine. *Geology*, 10(12), 611–616. [https://doi.org/10.1130/0091-7613\(1982\)10<611:petian>2.0.co;2](https://doi.org/10.1130/0091-7613(1982)10<611:petian>2.0.co;2)
- Tarantola, A. (1988). Theoretical background for the inversion of seismic waveforms, including elasticity and attenuation. In *Scattering and attenuations of seismic waves, part i* (pp. 365–399). Birkhäuser Basel. [https://doi.org/10.1007/978-3-0348-7722-0\\_19](https://doi.org/10.1007/978-3-0348-7722-0_19)
- Tarantola, A. (2005). *Inverse problem theory and methods for model parameter estimation*. SIAM.
- Thrustarson, S., van Driel, M., Krischer, L., Boehm, C., Afanasiev, M., van Herwaarden, D.-P., & Fichtner, A. (2020). Accelerating numerical wave propagation by wavefield adapted meshes. Part II: Full-waveform inversion. *Geophysical Journal International*, 221(3), 1591–1604. <https://doi.org/10.1093/gji/ggaa065>
- Thrustarson, S., van Herwaarden, D.-P., & Fichtner, A. (2021a). *Inversionson: Fully automated seismic waveform inversions*. California Digital Library (CDL). <https://doi.org/10.31223/x5f31v>
- Thrustarson, S., van Herwaarden, D.-P., Krischer, L., & Fichtner, A. (2021b). LASIF: LArge-scale seismic inversion framework, an updated version. <https://doi.org/10.31223/x5nc84>
- Tromp, J., Tape, C., & Liu, Q. (2005). Seismic tomography, adjoint methods, time reversal, and banana-doughnut kernels. *Geophysical Journal International*, 160(1), 195–216. <https://doi.org/10.1111/j.1365-246x.2004.02453.x>
- van Herwaarden, D. P., Afanasiev, M., Thrustarson, S., & Fichtner, A. (2021). Evolutionary full-waveform inversion. *Geophysical Journal International*, 224(1), 306–311. <https://doi.org/10.1093/gji/ggaa459>
- van Herwaarden, D. P., Boehm, C., Afanasiev, M., Thrustarson, S., Krischer, L., Trampert, J., & Fichtner, A. (2020). Accelerated full-waveform inversion using dynamic mini-batches. *Geophysical Journal International*, 221(2), 1427–1438. <https://doi.org/10.1093/gji/ggaa079>
- van Leeuwen, T., & Herrmann, F. J. (2013). Fast waveform inversion without source-encoding. *Geophysical Prospecting*, 61(s1), 10–19. <https://doi.org/10.1111/j.1365-2478.2012.01096.x>
- Virieux, J., & Operto, S. (2009). An overview of full-waveform inversion in exploration geophysics. *Geophysics*, 74(6), WCC1–WCC26. <https://doi.org/10.1190/1.3238367>
- Wessel, P., Smith, W. H. F., Scharroo, R., Luis, J., & Wobbe, F. (2013). Generic mapping tools: Improved version released. *Eos, Transactions American Geophysical Union*, 94(45), 409–410. <https://doi.org/10.1002/2013eo450001>
- Wu, J., Suppe, J., Lu, R., & Kanda, R. (2016). Philippine Sea and East Asian plate tectonics since 52 ma constrained by new subducted slab reconstruction methods. *Journal of Geophysical Research: Solid Earth*, 121, 4670–4741. <https://doi.org/10.1002/2016jb012923>
- Yao, H., van Der Hilst, R. D., & de Hoop, M. V. (2006). Surface-wave array tomography in SE Tibet from ambient seismic noise and two-station analysis — I. Phase velocity maps. *Geophysical Journal International*, 166(2), 732–744. <https://doi.org/10.1111/j.1365-246x.2006.03028.x>
- Yin, A. (2010). Cenozoic tectonic evolution of Asia: A preliminary synthesis. *Tectonophysics*, 488(1), 293–325. (Extensional Tectonics in the Basin and Range, the Aegean, and Western Anatolia). <https://doi.org/10.1016/j.tecto.2009.06.002>
- Zaroli, C., Koelemeijer, P., & Lambotte, S. (2017). Toward seeing the Earth's interior through unbiased tomographic lenses. *Geophysical Research Letters*, 44(22), 11399–11408. <https://doi.org/10.1002/2017gl074996>
- Zhang, Y., Yu, K., Fan, T., Yue, Y., Wang, R., Jiang, W., et al. (2020). Geochemistry and petrogenesis of quaternary basalts from Weizhou Island, northwestern south China sea: Evidence for the Hainan plume. *Lithos*, 362–363, 105493. <https://doi.org/10.1016/j.lithos.2020.105493>
- Zhao, D. (2004). Global tomographic images of mantle plumes and subducting slabs: Insight into deep Earth dynamics. *Physics of the Earth and Planetary Interiors*, 146(1), 3–34. <https://doi.org/10.1016/j.pepi.2003.07.032>
- Zhao, D., Hasegawa, A., & Horiuchi, S. (1992). Tomographic imaging of P and S wave velocity structure beneath northeastern Japan. *Journal of Geophysical Research*, 97(B13), 19909–19928. <https://doi.org/10.1029/92jb00603>
- Zheng, S., Sun, X., Song, X., Yang, Y., & Ritzwoller, M. H. (2008). Surface wave tomography of China from ambient seismic noise correlation. *Geochemistry, Geophysics, Geosystems*, 9(5), Q05020. <https://doi.org/10.1029/2008gc001981>



- Zheng, X.-F., Yao, Z.-X., Liang, J.-H., & Zheng, J. (2010). The role played and opportunities provided by IGP DMC of China National Seismic Network in Wenchuan earthquake disaster relief and researches. *Bulletin of the Seismological Society of America*, *100*(5B), 2866–2872. <https://doi.org/10.1785/0120090257>
- Zheng, Y.-F., Xiao, W.-J., & Zhao, G. (2013). Introduction to tectonics of China. *Gondwana Research*, *23*(4), 1189–1206. <https://doi.org/10.1016/j.gr.2012.10.001>
- Zhu, H., Bozdağ, E., Peter, D., & Tromp, J. (2012). Structure of the European upper mantle revealed by adjoint tomography. *Nature Geoscience*, *5*(7), 493–498. <https://doi.org/10.1038/ngeo1501>
- Zhu, H., Komatitsch, D., & Tromp, J. (2017). Radial anisotropy of the North American upper mantle based on adjoint tomography with USArray. *Geophysical Journal International*, *211*(1), 349–377. <https://doi.org/10.1093/gji/ggx305>